




## RESEARCH ARTICLE

# Myelinated peripheral axons are more vulnerable to mechanical trauma in a model of enlarged axonal diameters

Vasiliki-Ilya Gargareta<sup>1</sup>  | Stefan A. Berghoff<sup>1</sup>  | Doris Krauter<sup>1</sup>  |  
Sophie Hümmert<sup>1</sup>  | Katy L. H. Marshall-Phelps<sup>2</sup>  | Wiebke Möbius<sup>1</sup>  |  
Klaus-Armin Nave<sup>1</sup>  | Robert Fledrich<sup>1</sup>  | Hauke B. Werner<sup>1,3</sup>  |  
Maria A. Eichel-Vogel<sup>1,2</sup> 

<sup>1</sup>Department of Neurogenetics, Max Planck Institute for Multidisciplinary Sciences, Göttingen, Germany

<sup>2</sup>Centre for Discovery Brain Sciences, University of Edinburgh, Edinburgh, UK

<sup>3</sup>Institute of Neuronal Cell Biology, Technical University, Munich, Germany

**Correspondence**

Hauke B. Werner and Maria A. Eichel-Vogel, Department of Neurogenetics, Max Planck Institute for Multidisciplinary Sciences, D-37075 Göttingen, Germany.  
Email: [hauke@mpinat.mpg.de](mailto:hauke@mpinat.mpg.de) and [maria.eichelvogel@ed.ac.uk](mailto:maria.eichelvogel@ed.ac.uk)

**Present addresses**

Stefan A. Berghoff, Institute of Neuronal Cell Biology, Technical University Munich, Munich, Germany; Doris Krauter, Division of Molecular Neurobiology, Department of Medical Biochemistry and Biophysics, Karolinska Institute, Stockholm, Sweden; and Robert Fledrich, Institute of Anatomy, University of Leipzig, Leipzig, Germany.

**Funding information**

Deutsche Forschungsgemeinschaft, Grant/Award Numbers: 493410640, WE 2720/5-1

**Abstract**

The velocity of axonal impulse propagation is facilitated by myelination and axonal diameters. Both parameters are frequently impaired in peripheral nerve disorders, but it is not known if the diameters of myelinated axons affect the liability to injury or the efficiency of functional recovery. Mice lacking the adaxonal myelin protein chemokine-like factor-like MARVEL-transmembrane domain-containing family member-6 (CMTM6) specifically from Schwann cells (SCs) display appropriate myelination but increased diameters of peripheral axons. Here we subjected *Cmtm6*-cKo mice as a model of enlarged axonal diameters to a mild sciatic nerve compression injury that causes temporarily reduced axonal diameters but otherwise comparatively moderate pathology of the axon/myelin-unit. Notably, both of these pathological features were worsened in *Cmtm6*-cKo compared to genotype-control mice early post-injury. The increase of axonal diameters caused by CMTM6-deficiency thus does not override their injury-dependent decrease. Accordingly, we did not detect signs of improved regeneration or functional recovery after nerve compression in *Cmtm6*-cKo mice; depleting CMTM6 in SCs is thus not a promising strategy toward enhanced recovery after nerve injury. Conversely, the exacerbated axonal damage in *Cmtm6*-cKo nerves early post-injury coincided with both enhanced immune response including foamy macrophages and SCs and transiently reduced grip strength. Our observations support the concept that larger peripheral axons are particularly susceptible toward mechanical trauma.

**KEYWORDS**

axon diameter, axon/glia interaction, CMTM6, myelin, peripheral nerve injury, Schwann cell

Vasiliki-Ilya Gargareta and Maria A. Eichel-Vogel contributed equally to this work.

This is an open access article under the terms of the [Creative Commons Attribution-NonCommercial](https://creativecommons.org/licenses/by-nc/4.0/) License, which permits use, distribution and reproduction in any medium, provided the original work is properly cited and is not used for commercial purposes.

© 2024 The Authors. GLIA published by Wiley Periodicals LLC.

## 1 | INTRODUCTION

Following injury, regeneration of the peripheral nervous system (PNS) is slow and often incomplete, notwithstanding that its regenerative capacity is higher compared with the central nervous system (CNS) (Lutz & Barres, 2014). Recovery of the PNS has been mainly attributed to the close interactions between axons and Schwann cells (SCs), the myelin-forming cells of the PNS, and their remarkable plasticity upon injury (Jessen & Arthur-Farraj, 2019; Stassart & Woodhoo, 2021). In acutely injured peripheral nerves, that is, upon neurotmesis (nerve cut) or axonotmesis (nerve crush), axons in the distal part of the nerve undergo Wallerian degeneration, and their debris is cleared rapidly. Independent of the injury type, SCs respond to the injury and undergo well-defined morphological and molecular changes that reflect their trans-differentiation into repair SCs (Arthur-Farraj et al., 2012; Fontana et al., 2012; Jessen & Mirsky, 2016). Indeed, repair SCs not only recruit macrophages to the injury site but also actively contribute to myelin clearance via (auto)phagocytosis and myelinophagy (Gomez-Sanchez et al., 2015; Jang et al., 2016; Lutz et al., 2017; Stratton & Shah, 2016), release neurotrophic factors to support neuronal survival, guide axonal regrowth by forming regeneration tracts, interact with the extracellular matrix, and ultimately redifferentiate to remyelinate axons (Chen et al., 2007; Jessen & Arthur-Farraj, 2019; Madduri & Gander, 2010; Nocera & Jacob, 2020).

However, especially in humans, full functional recovery is rarely achieved and can be slowed down during aging (Höke, 2006; Painter et al., 2014; Scheib & Höke, 2016; Wagstaff et al., 2021). Limitations of nerve repair include insufficient axonal regrowth and reinnervation, misrouting of axons, insufficient regrowth of axonal diameters, lower number of SCs, shorter internodes, insufficient remyelination, and impaired reconstitution of axonal diameters—all parameters that may contribute to slowed nerve conduction velocity (NCV) and compromised regeneration, which in turn can cause persistent muscle denervation (Li et al., 2019; Schröder, 1972; Stassart et al., 2013; Tseng et al., 2016; Vaughan, 1992; Verdú et al., 2000). Notably, models of both chronic nerve compression and demyelinating neuropathies display a shift toward smaller axonal diameters, which has been hypothesized to arise from a loss of larger myelinated axons, an assumption that is formally unproven yet (Bilbao & Schmidt, 2015; Gupta & Steward, 2003; O'Brien et al., 1987; Vavlitou et al., 2010).

Several studies have shown that interfering with SC function, particularly those that impact the bidirectional SC–axon interaction, leads to impaired axonal regeneration, remyelination, and functional recovery (Jessen & Mirsky, 2019; Quintes et al., 2016; reviewed in Stassart & Woodhoo, 2021; Xiao et al., 2015). Nonetheless, the functional relevance of molecules that may facilitate the interactions between SCs and axons toward functional recovery has remained incompletely understood. We previously reported that chemokine-like factor-like MARVEL-transmembrane domain-containing family member-6 (CMTM6) is expressed on the adaxonal SC surface and involved in the function of SCs to restrict axonal diameters in peripheral nerves (Eichel et al., 2020). Indeed, non-injured mice lacking CMTM6 from

SCs (*Cmtm6*-cKo mice) show increased axonal diameters already at 1 month of age and accelerated sensory NCV in peripheral nerves. Importantly, myelin sheath thickness is appropriate, and axonal integrity is not impaired in *Cmtm6*-cKo mice.

Here, we use this genetic model to test if increasing axonal diameters via depleting CMTM6 in SCs could enhance functional recovery after nerve compression. As an alternative hypothesis, we test if larger axons are more susceptible to mechanical injury. We hypothesize that the vulnerability of large axons contributes to the previously observed shift in diameter distributions toward smaller axonal diameters after nerve injury (Goodrum et al., 2000; Ikeda & Oka, 2012; Li et al., 2019; Schröder, 1972; Stassart et al., 2013; Tseng et al., 2016). To test these hypotheses, we developed a comparatively mild sciatic nerve compression model that does not result in complete degeneration of axons in the entire nerve. We applied this model to *Cmtm6*-cKo and control mice and assessed morphological and functional changes up to 8 weeks non-injured. Indeed, we find that genotype-control mice upon mild nerve compression display less axonal degeneration compared with conventional sciatic nerve crush injury models; yet up to 20% of myelinated axons develop pathological signs coinciding with a shift toward smaller axonal diameters and mild functional impairment early non-injured. Notably, *Cmtm6*-cKo compared to genotype control mice early non-injured displayed enhanced neuropathology including even further reduced axonal diameters. The expected genotype-dependent increase in axonal diameters does only reappear at 8 weeks non-injured. Considering the worsened neuropathology and the absence of ameliorated functional recovery in *Cmtm6*-cKo mice, depleting CMTM6-expression in SCs is not a suitable therapeutic strategy toward enhanced functional recovery after injury. Yet, our data support the concept that larger axons are more vulnerable to mechanical trauma.

## 2 | RESULTS

### 2.1 | Mild nerve compression causes reduced axonal diameters, moderate axonal pathology, and mild functional impairment in genotype-control mice

We aimed to establish a mild nerve injury model that results in reduced axonal diameters but only moderate axonal pathology. Using flat tweezers, we compressed the sciatic nerve below the sciatic notch of the left hind limb for 15 s at 10 weeks of age in genotype-control mice (genotype *Cmtm6*<sup>fl<sup>ox</sup>/fl<sup>ox</sup></sup>) and characterized the injury response (see overview in Figure 1a). To assess the progression of nerve repair, we employed molecular, morphological, and functional analyses at five time points after injury (3, 7, 14, 28 and 56 days post-compression [dpc]) (see scheme in Figure 1a). For molecular and morphological analyses, we dissected nerve segments distal to the compression site and additionally collected the contralateral sciatic nerve as non-injured control.

By light microscopic observation of semithin-sectioned sciatic nerves, compared to non-injured nerves (exemplified in Figure 1b), we

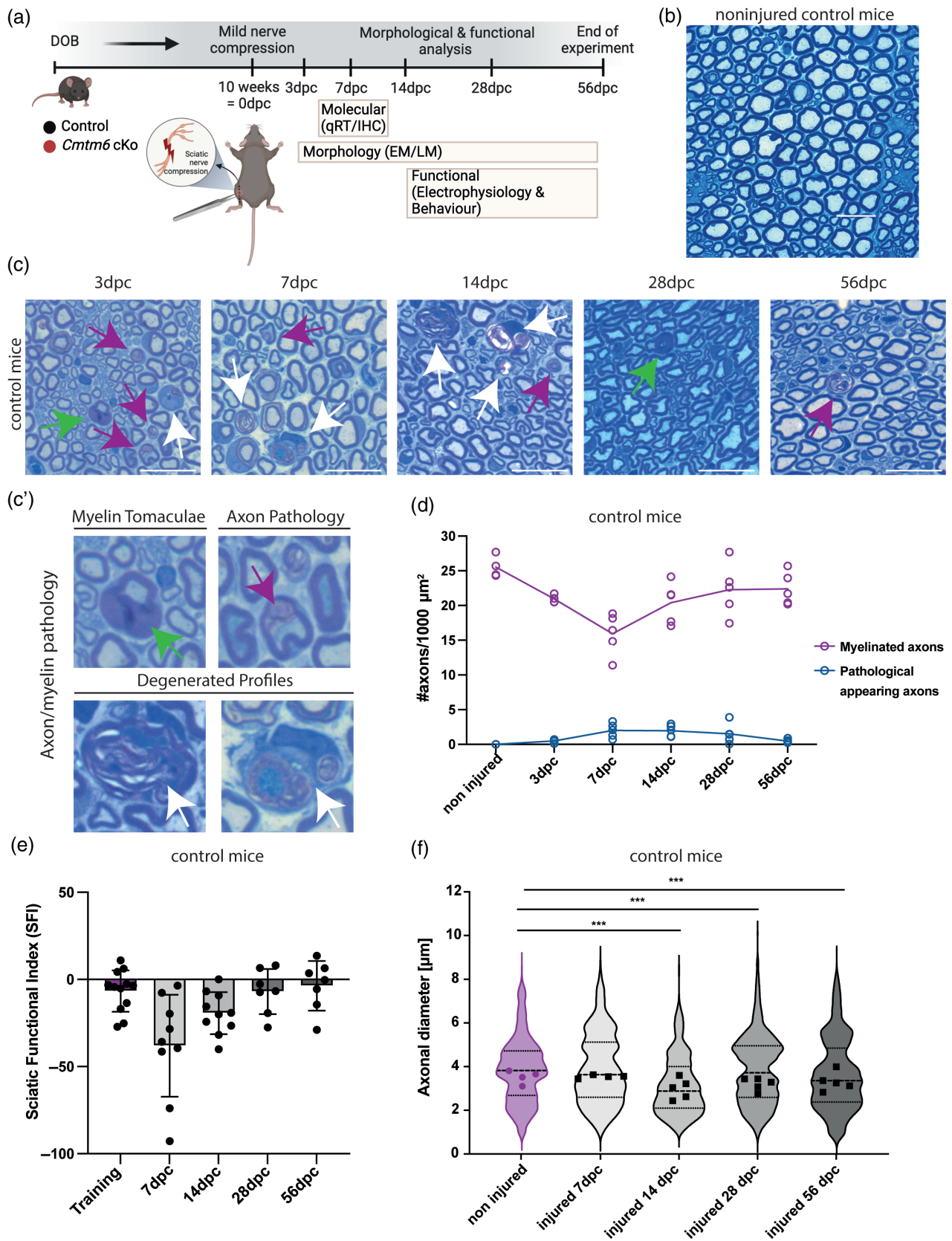


FIGURE 1 Legend on next page.

observed an increase in the number of pathological-appearing axons and a loss of normal myelinated axons per defined area 7–14 dpc, both of which gradually normalize by 56 dpc (Figure 1c,c',d). This coincided with a decrease of the Sciatic Function Index (SFI) 7 dpc and subsequent recovery (Figure 1e). By quantitative assessment of axonal diameters on light micrographs, we observed an injury-dependent shift toward smaller axonal diameters that was most prominent at 14 dpc (Figure 1f, Figure S1B) and did not fully recover by 56 dpc (Figure 1f, Figure S1C,D). Different from injured controls, injured nerves at 14 dpc displayed a reduced number specifically of axons with a diameter  $\geq 4.5 \mu\text{m}$ , and axons with a diameter of  $\geq 7.5 \mu\text{m}$  were largely absent (Figure S1B). Our mild sciatic nerve compression injury model thus involves comparatively few pathological-appearing axons but a considerable shift toward smaller axonal diameters.

## 2.2 | Mild nerve compression in *Cmtm6*-cKo mice results in further reduced axonal diameters and enhanced axonal pathology compared to genotype-control mice

After establishing our mild nerve compression model, we aimed to test if larger axons are more susceptible to mechanical injury. Without injury, *Cmtm6*-cKo mice (genotype *Cmtm6*<sup>flox/flox</sup>\**Dhh*<sup>Cre</sup>) display a shift toward larger axonal diameters (1) in various non-injured peripheral nerves including the sciatic nerve and (2) at multiple developmental stages (Eichel et al., 2020), including the time point at which injury was induced in the present study. We thus subjected both *Cmtm6*-cKo mice and genotype-control mice (genotype *Cmtm6*<sup>flox/flox</sup>) to sciatic nerve compression (see scheme in Figure 1a; see data in Figures 2–4 and S2–

S5). We note that the injured genotype-control cohort in Figures 2–4 and S2–S5 comprises the same group of injured mice as displayed in Figure 1. When assessing axonal diameters in sciatic nerves by light microscopy 7, 14, 28, and 56 dpc, *Cmtm6*-cKo mice displayed a shifted frequency toward larger axonal diameters only at 56 dpc (Figure 2g); the genotype-dependent increase of axonal diameters in the present experiment was essentially similar in extent as previously reported for non-injured sciatic nerves at 2 months of age (mean axonal diameter  $\text{ctrl} \pm \text{Cmtm6-cKo} = 3.40 \pm 0.09$ ; Eichel et al., 2020). However, at 28 dpc, injured *Cmtm6*-cKo nerves displayed similar axonal diameters as injured genotype-controls (Figure 2e). Moreover, strikingly, at 7 and 14 dpc, we found a significant shift of frequency distribution toward smaller axonal diameters in *Cmtm6*-cKo compared to control nerves (Figure 2a,c). Thus, when comparing injured genotype-control to *Cmtm6*-cKo nerves, the latter displayed a reduced frequency of axons with diameters of  $\geq 4.5 \mu\text{m}$  as early as 7 dpc that continued to be significant at 14 dpc (Figure 2a,c) and normalized by 28 dpc (Figure 2e); by 56 dpc the genotype-dependent increase of axonal diameters caused by *CMTM6*-deficiency in SCs (Figure 2g) was re-established as previously reported (Eichel et al., 2020).

We also used these light micrographs to determine the myelination status and pathology of axons in *Cmtm6*-cKo compared to control sciatic nerves after compression at 7, 14, 28, and 56 dpc. It is of note that non-injured *Cmtm6*-cKo mice display appropriate myelination and unimpaired axonal integrity (Eichel et al., 2020). At 7 dpc, we observed that the number of myelinated axons per area in *Cmtm6*-cKo mice was significantly decreased, whereas the number of pathological-appearing axons was increased compared with control mice (Figure 2b). At 14 dpc, *Cmtm6*-cKo mice displayed a nonsignificant trend toward a reduced number of myelinated axons and an increased

**FIGURE 1** Mild nerve compression model with moderate axonal pathology and reduced axonal diameters. (a) Scheme depicting the timeline of mild sciatic nerve compression experiments in genotype control and *Cmtm6*-cKo mice. Ten weeks after birth, mice underwent surgery for induction of sciatic nerve compression in their left hind limb. Mice were assessed at various time points up to 56 days post-compression (dpc) by behavioral tests and electrophysiology to evaluate functional performance (see Figures S3 and S4). Sciatic nerve segments distal to the compression site of both genotypes and non-injured control nerves were dissected at several time points and assessed by qRT-PCR (qRT), immunohistochemistry (IHC), and electron and light microscopy (EM/LM). (b) Representative micrograph of a semithin cross-sectioned, non-injured sciatic nerve of a genotype-control mouse. Scale bar, 20  $\mu\text{m}$ . (c) Representative semithin micrographs of cross-sectioned sciatic nerves 3, 7, 14, 28, and 56 dpc. Note the progressive neuropathology early post-compression (3, 7, and 14 dpc) in genotype-control mice (genotype *Cmtm6*<sup>flox/flox</sup>). Magenta arrows point at axonal pathology, green arrows point at myelin tomaculae, and white arrows point at degenerated profiles that are recognizable from the myelin debris and the lack of an axonal compartment. These categories were quantified and summarized as pathological-appearing axons; for quantification, see (e). Scale bars, 20  $\mu\text{m}$ . (c') Magnifications of pathological features described in (c). (d) Plot showing the number of myelinated and pathological-appearing axons per 1000  $\mu\text{m}^2$  as quantified on whole sciatic nerve semithin sections at 3, 7, 14, 28, and 56 dpc in genotype-control mice (*Cmtm6*<sup>flox/flox</sup>). Note the reduced number of myelinated axons early post-injury reaching its minimum 7 dpc coinciding with an increase in pathological-appearing axons. Both normalize over time. Data points indicate individual mice;  $n = 4$  non-injured mice and  $n = 5$  injured mice at each time point. (e) Bar graph showing Sciatic Functional Index (SFI) as measured at the left hind paw using the Catwalk™ system to assess functional recovery of genotype-control mice (*Cmtm6*<sup>flox/flox</sup>) after mild nerve compression. Note that values of 0 are considered normal while  $-100$  would indicate that a mouse does not use its left hind limb. Mean  $\pm$  SD; Data points indicate individual mice; training day  $n = 12$ ; 7 dpc  $n = 9$ ; 14 dpc  $n = 10$ ; 28 dpc  $n = 7$ ; 56 dpc  $n = 7$ . (f) Violin plot showing axonal diameter distributions in sciatic nerves at 7, 14, 28, and 56 compared with non-injured control mice quantified on whole sciatic nerve semithin sections. Circles and squares indicate mean axonal diameters in individual mice; stippled lines indicate median and quartiles. Note the higher density of smaller diameters early post-injury and the overall smaller mean axonal diameters at 14, 28, and 56 compared with non-injured control mice. Overall, 11,553 axons were from  $n = 4$  non-injured mice, 6349 axons from  $n = 4$  injured mice at 7 dpc, 9715 axons from  $n = 5$  injured mice at 14 dpc, 12,784 axons from  $n = 5$  injured mice at 28 dpc, and 9623 axons from  $n = 5$  injured mice at 56 dpc. For frequency distribution of binned axonal diameters for each time point and statistical assessment, see Figure S1. DOB, date of birth.

number of pathological-appearing axons (Figure 2d). No genotype-dependent differences regarding axonal pathology or myelination status were observed at 28 and 56 dpc (Figure 2f,h).

Considering that myelin sheath thickness depends on the diameters of the underlying axons (Michailov et al., 2004; Taveggia et al., 2005) and is reduced after nerve injury (Li et al., 2019; Schröder, 1972; Stassart et al., 2013; Tseng et al., 2016), we assessed the ratio between myelin sheath thickness and axon diameter (g-ratio) on electron micrographs of cross-sectioned sciatic nerves at 7 and 56 dpc. We find that the g-ratio was unaltered (Figure S2A,B), indicating appropriate myelin sheath thickness of healthy-appearing myelinated axons in *Cmtm6*-cKo mice both without (Eichel et al., 2020) and after nerve injury (Figure S2A,B).

Together, the injury-dependent shift toward smaller axonal diameters, and the presence of axonal pathology early post-injury was

exacerbated in *Cmtm6*-cKo compared to genotype-control nerves but normalized over time. By 56 dpc, the CMTM6-deficiency-dependent increase of axonal diameters was re-established to the extent previously observed in non-injured *Cmtm6*-cKo nerves (Eichel et al., 2020). It is plausible that the injury-dependent reduction of axonal diameters at early stages after nerve compression is driven by an increased sensitivity of larger axons toward mechanical trauma.

### 2.3 | CMTM6 deficiency does not improve functional recovery after nerve compression

To test if functional recovery after nerve compression differs between *Cmtm6*-cKo and control mice, we performed multiple assays measuring behavioral capabilities (grip strength, hotplate, and grid test; for

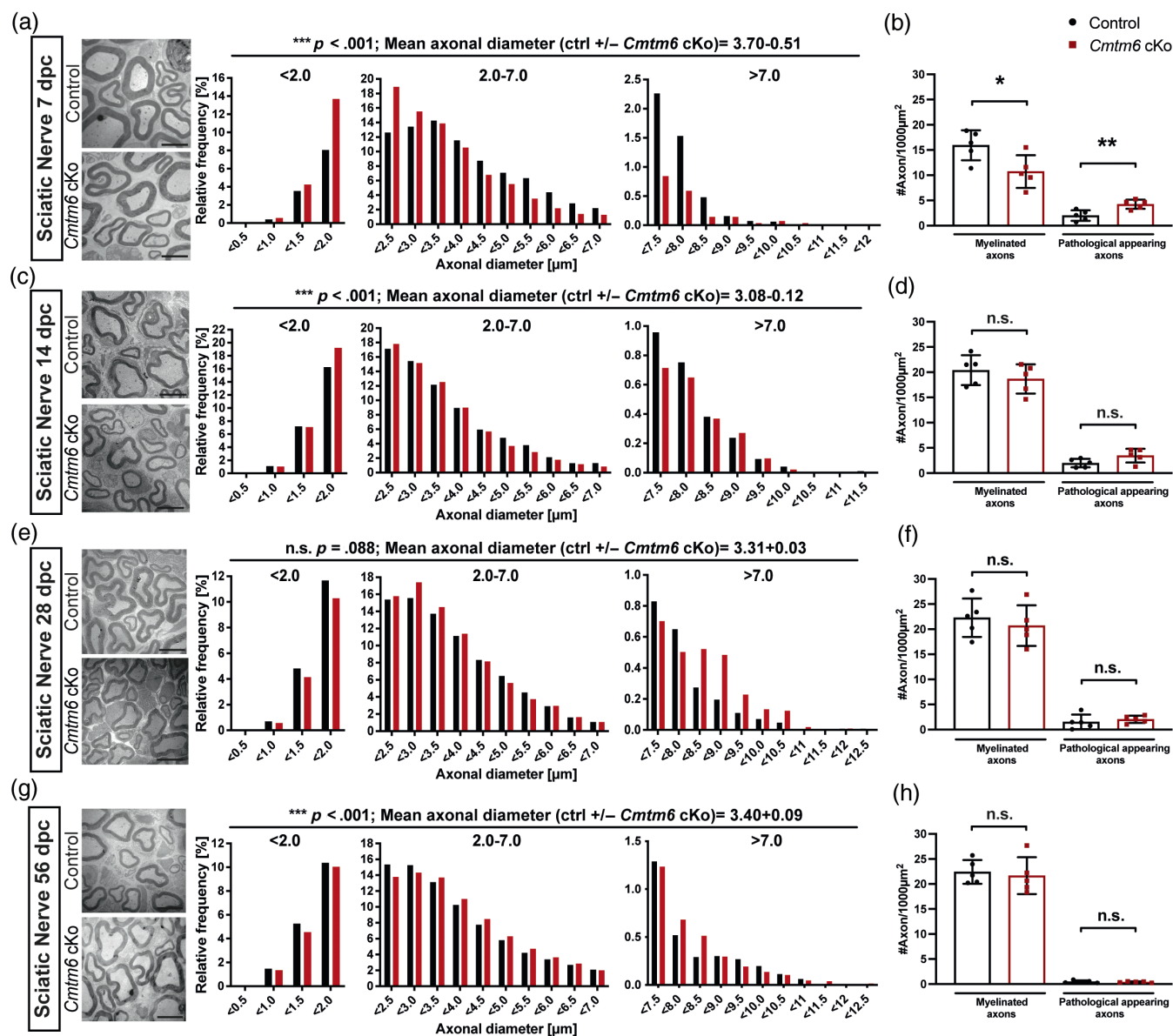


FIGURE 2 Legend on next page.

timeline see Figure 1a). However, we did not find evidence for accelerated or improved functional recovery of *Cmtm6*-cKo compared to control mice (Figure S3A–C). On the contrary, grip strength of the hind limbs was moderately but significantly decreased in *Cmtm6*-cKo compared with control mice 14 dpc, while normalizing by 28 and 56 dpc. This indicates a moderate transient impairment of motor capabilities in injured mice when lacking CMTM6 from SCs.

Since motor performance is enabled by signaling via large myelinated fibers, the reduced axonal diameters and loss of predominantly large axons (>4.5  $\mu\text{m}$ ) in *Cmtm6*-cKo mice upon injury (Figure 2) likely contributes to this observation. Using the CatWalk™ system to assess gait and locomotor parameters as a readout for functional recovery after nerve compression (Heinzel et al., 2020), we did not observe considerable differences between *Cmtm6*-cKo and control mice, neither at baseline during training nor at various time points after compression (Figure S4). When using electrophysiology to measure motor and sensory NCV at 14, 28, and 56 dpc, we did not observe genotype-dependent differences (Figure S3D,E). Deleting CMTM6 from SCs thus does not improve or accelerate recovery after sciatic nerve compression.

## 2.4 | CMTM6 protein localization and mRNA expression early post-injury

Previously published transcriptional profile datasets of crushed sciatic nerves in both rats and mice showed a decrease in *Cmtm6* mRNA abundance (Lutz et al., 2022; Yi et al., 2015). This prompted us to evaluate expression of CMTM6 in our mild nerve compression model

by assessing its protein localization and mRNA abundance 7 dpc (Figure S5).

By immunohistochemistry of cross-sectioned non-injured sciatic nerves of genotype control mice (*Cmtm6*<sup>flox/flox</sup>), CMTM6 immunolabeling (yellow in Figure S5A) was detected toward the inside of the compact myelin compartment (autofluorescence in blue in Figure S5A), reflecting its localization in the adaxonal myelin membrane (arrowheads in Figure S5A) as previously reported (Eichel et al., 2020). Upon injury, however, CMTM6 immunolabeling was additionally detected toward the outside of the compact myelin compartment, suggesting partial redistribution to the abaxonal myelin layer (stars in Figure S5A). Therefore, upon injury, CMTM6 is not confined to the adaxonal myelin layer but partially redistributed to the abaxonal myelin surface.

We then used quantitative real-time PCR (qRT-PCR) to test the relative abundance of marker transcripts in injured nerves 7 dpc of both genotypes compared to non-injured control nerves. First, we detected the expected genotype-dependent decrease in the abundance of *Cmtm6* mRNA in *Cmtm6*-cKo compared with genotype control nerves (Figure S5C). More interestingly, both *Cmtm6*-cKo and genotype control nerves 7 dpc displayed a markedly reduced abundance of *Cmtm6* mRNA compared to non-injured nerves (Figure S5B, C), in agreement with previously published datasets (Lutz et al., 2022; Yi et al., 2015). This confirms that early upon injury, the expression of *Cmtm6* mRNA is indeed downregulated.

When using qRT-PCR to assess other marker transcripts commonly changed after nerve injuries in more severely affected models including nerve crush, we found that our mild model involves a similar injury-dependent reduction of the relative abundance of myelination-related mRNAs (*Mag* and *Pmp22*), increase of transcripts encoding

**FIGURE 2** Axon diameter distribution shift toward smaller diameters in *Cmtm6*-cKo early post nerve compression. (a) Representative electron micrographs of cross-sectioned, injured sciatic nerves and genotype-dependent quantifications at 7 dpc reveals frequency distribution shift toward smaller axonal diameters in *Cmtm6*-cKo compared with control mice. Data presented as frequency distribution with 0.5  $\mu\text{m}$  bin width; 8358 axons in  $n = 5$  control and 5582 axons in  $n = 5$  *Cmtm6*-cKo; mean axonal diameter ( $_{\text{control}} \pm \text{Cmtm6-cKo}$ ) = 3.70 – 0.51  $\mu\text{m}$ ;  $p < .0001$  by two-sided Kolmogorow–Smirnow test of frequency distributions. Scale bar, 2.5  $\mu\text{m}$ . (b) Quantitative assessment of axonal numbers/1000  $\mu\text{m}^2$  sciatic nerve area shows decreased number of myelinated axons and increased number of pathological-appearing axons in *Cmtm6*-cKo compared with control mice 7 dpc. Myelinated axons:  $p = .029$ ; pathological-appearing axons:  $p = .006$  by two-tailed Student's *t*-test. (c) Representative electron micrographs of injured sciatic nerves 14 dpc and genotype-dependent quantification reveals persisting frequency distribution shift toward smaller axonal diameters in *Cmtm6*-cKo compared with control mice. Data presented as frequency distribution with 0.5  $\mu\text{m}$  bin width; 9715 axons in  $n = 5$  control, and 9249 axons in  $n = 5$  *Cmtm6*-cKo; mean axonal diameter ( $_{\text{control}} \pm \text{Cmtm6-cKo}$ ) = 3.08 – 0.12  $\mu\text{m}$ ;  $p < .0001$  by two-sided Kolmogorow–Smirnow test of frequency distributions. Scale bar, 2.5  $\mu\text{m}$ . (d) Quantitative assessment of axonal numbers/1000  $\mu\text{m}^2$  sciatic nerve area shows similar numbers of myelinated and pathological-appearing axons in *Cmtm6*-cKo and control mice at 14 dpc. Myelinated axons:  $p = .378$ ; pathological-appearing axons:  $p = .072$  by two-tailed Student's *t*-test. (e) Representative electron micrographs of injured sciatic nerves 28 and genotype-dependent quantification reveals similar frequency distribution of axonal diameters in *Cmtm6*-cKo and control mice. Data presented as frequency distribution with 0.5  $\mu\text{m}$  bin width; 12,784 axons in  $n = 5$  control and 10,534 axons in  $n = 5$  *Cmtm6*-cKo; mean axonal diameter ( $_{\text{control}} \pm \text{Cmtm6-cKo}$ ) = 3.31 + 0.03  $\mu\text{m}$ ;  $p = .088$  by two-sided Kolmogorow–Smirnow test of frequency distributions. Scale bar, 2.5  $\mu\text{m}$ . (f) Quantitative assessment of axonal numbers/1000  $\mu\text{m}^2$  sciatic nerve area shows similar numbers of myelinated and pathological-appearing axons in *Cmtm6*-cKo compared with control mice 28 dpc. Myelinated axons:  $p = .552$ ; pathological-appearing axons:  $p = .496$  by two-tailed Student's *t*-test. (g) Representative electron micrographs of injured sciatic nerves 56 dpc and genotype-dependent quantification reveal a frequency distribution shift toward larger axonal diameters in *Cmtm6*-cKo compared with control mice. Data presented as frequency distribution with 0.5  $\mu\text{m}$  bin width; 9623 axons in  $n = 5$  control and 12,471 axons in  $n = 5$  *Cmtm6*-cKo; mean axonal diameter ( $_{\text{control}} \pm \text{Cmtm6-cKo}$ ) = 3.40 + 0.09  $\mu\text{m}$ ;  $p < .0001$  by two-sided Kolmogorow–Smirnow test of frequency distributions. Scale bar, 2.5  $\mu\text{m}$ . (h) Quantitative assessment of axonal numbers/1000  $\mu\text{m}^2$  sciatic nerve area shows similar numbers of myelinated and pathological-appearing axons in *Cmtm6*-cKo compared with control mice 56 dpc. Myelinated axons:  $p = .713$ ; pathological-appearing axons:  $p = .573$  by two-tailed Student's *t*-test. Data in b, d, f, and h presented as mean  $\pm$  SD;  $n = 5$  mice per genotype; n. s. = nonsignificant  $p > .05$ ; \* $p < .05$ ; \*\* $p < .01$ .

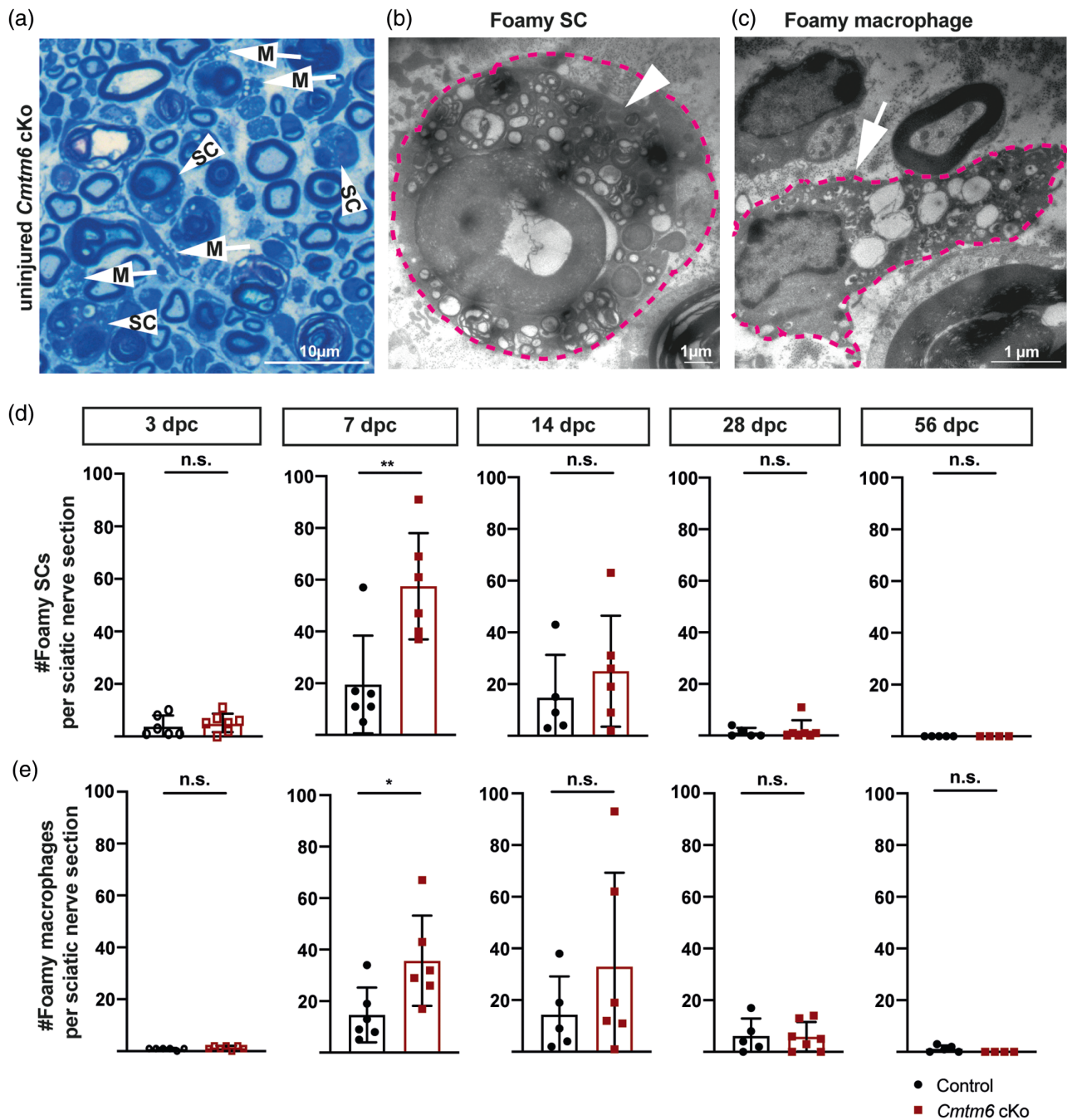


**FIGURE 3** Increased number of foamy macrophages and Schwann cells (SC) in *Cmtm6*-cKo nerves early post-injury. (a) Representative light micrograph of a toluidine-blue stained semithin cross-section of a *Cmtm6*-cKo sciatic nerve 7 dpc. White arrowheads point at foamy SC as quantified in (d). White arrows indicate foamy, lipid-loaded macrophages (M) as quantified in Figure 3e. Scale bar 10  $\mu$ m. (b) Representative electron micrograph of a foamy SC (encircled in magenta, white arrow) in a cross-sectioned sciatic nerve of a *Cmtm6*-cKo mouse 7 dpc. A roundish structure with myelin debris, lipid accumulations and a surrounding basal membrane are characteristic of foamy SC. Scale bar 1  $\mu$ m. (c) Representative electron micrograph of a foamy, lipid-loaded macrophage (encircled in magenta, white arrow) in a cross-sectioned sciatic nerve of a *Cmtm6*-cKo mouse 7 dpc. Elongated cells with evident nuclei and lipid and membrane accumulations are characteristic of foamy macrophages. Scale bar 1  $\mu$ m. (d) Genotype-dependent quantification of the number of foamy SC per sciatic nerve section shows a significant increase in *Cmtm6*-cKo compared with control mice 7 dpc. Data presented as mean  $\pm$  SD; data points represent individual mice;  $n = 4$ –7 per genotype; two-tailed Student's  $t$ -test; 3 dpc  $p = .595$ , 7 dpc  $p = .007$ , 14 dpc  $p = .408$ , 28 dpc  $p = .687$ , at 56 dpc all values are 0. (e) Genotype-dependent quantification of the number of foamy macrophages per nerve section shows a significant increase in *Cmtm6*-cKo compared with control mice 7 dpc. Data presented as mean  $\pm$  SD; data points represent individual mice;  $n = 4$ –7 per genotype; two-tailed Student's  $t$ -test; 3 dpc  $p = .218$ , 7 dpc  $p = .03$ , 14 dpc  $p = .314$ , 28 dpc  $p = .926$ , 56 dpc  $p = .112$ . n.s. = nonsignificant  $p > .05$ ; \* $p < .05$ ; \*\* $p < .01$ .

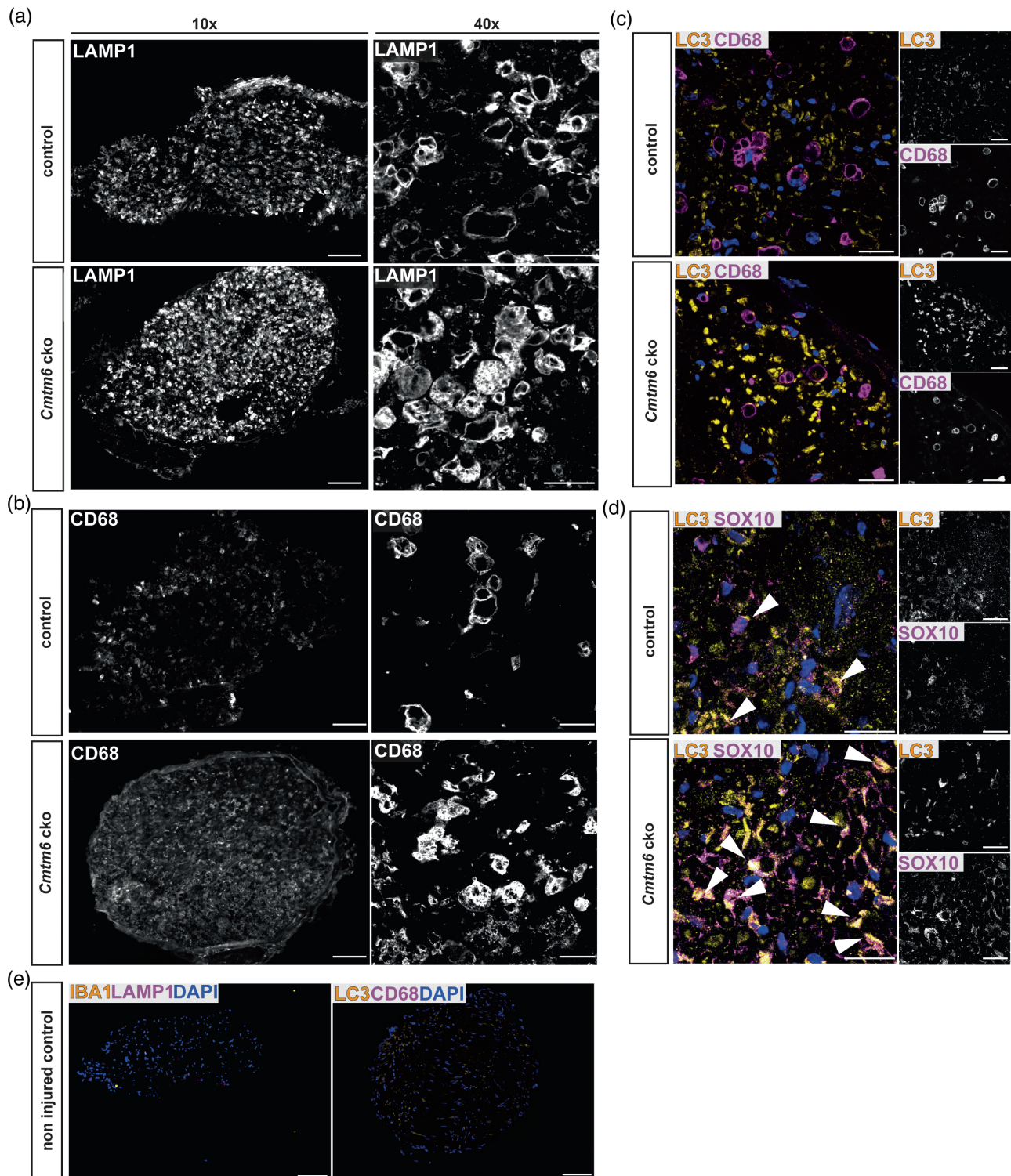


**FIGURE 4** Increased (auto)phagocytosis and lysosomal markers in *Cmtm6*-cKo mice 7 dpc. (a, b) Immunodetection of LAMP1 (lysosomal marker) and CD68 (lysosomal marker for macrophages) on cross-sectioned sciatic nerves 7 dpc imaged at 10 $\times$  (left) and 40 $\times$  (right) magnification. Note the higher intensity of LAMP1 (a) and CD68 (b) immunolabeling in *Cmtm6*-cKo compared with control mice. Scale bars for 10 $\times$  magnification images 100  $\mu$ m; scale bars for 40 $\times$  images 5  $\mu$ m. (c, d) Immunodetection of LC3 (yellow, marker for autophagocytosis) and CD68 (c, magenta, lysosomal marker for macrophages) or SOX10 (d, magenta, marker for Schwann cells) on cross-sectioned sciatic nerves 7 dpc. Note the higher intensity of LC3 labeling in *Cmtm6*-cKo compared with control mice. White arrowheads indicate Schwann cells immunopositive for both LC3 and SOX10 (d). Scale bars 5  $\mu$ m. (e) Immunolabeling of cross-sectioned sciatic nerves dissected from non-injured control mice shows that markers LAMP1, IBA1, CD68, and LC3 are virtually undetectable in non-injured sciatic nerves. Immunolabeling and microscopy were in parallel and using the same conditions as in (a–d). Images were taken at 10 $\times$  magnification, scale bars 100  $\mu$ m.



inhibitors of myelination (*Sox2* and *Jun*), as well as an increase in lipid export marker mRNAs (*ApoE* and *Abca1*) 7 dpc (Figure S5B). These data are in agreement with previously established datasets assessing transcriptional profiles upon peripheral nerve injuries (Lutz et al., 2022; Ydens et al., 2020; Yi et al., 2015).

When comparing injury-dependent mRNA abundance changes between *Cmtm6*-cKo and control sciatic nerves, most marker transcripts for SCs, phagocytosis, lipid export, and inflammation displayed similar abundance between the genotypes (Figure S5B). As an exception, we observed a moderate but significant genotype-dependent decrease in injured *Cmtm6*-cKo sciatic nerves compared with genotype controls of the relative abundance of transcripts (Figure S5B,D–F) encoding the myelin-specific, axon diameter-related myelin-associated glycoprotein (*Mag*) (Eichel et al., 2020; Yin et al., 1998), the phagocytosis marker *Cd36* (Grajchen et al., 2020), and the lipid export-related *Abca1* (Chinetti et al., 2001; Zhou et al., 2019).

These results show that mild nerve compression as applied here results in molecular responses analogous to other nerve injury models despite the differences in the extent of neuropathology.

## 2.5 | Increased number of foamy cells in *Cmtm6*-cKo nerves early post-injury

Considering the enhanced neuropathological reaction in *Cmtm6*-cKo compared to genotype control nerves early post-injury (Figure 2a,b), we extended their morphological assessment. At 7 dpc, both repair SCs and recruited macrophages actively break down myelin proteins and lipids, which enables clearance of the nerve ahead of regeneration (Chen et al., 2015; Jessen & Mirsky, 2019; Nocera & Jacob, 2020). Considering that the enlargement of axons by CMTM6-deficiency may cause increased vulnerability to the mechanical impact by nerve compression, thereby causing the presence of more breakdown products, we assessed SCs and macrophages. Indeed, at 7 and 14 dpc, the time when axonal regeneration and remyelination start taking place, we detected a considerable number of lipid- and debris-loaded cells, commonly referred to as foamy cells (Figure 3a). For quantification, we discriminated between foamy SCs (Figure 3b) and foamy macrophages (Figure 3c) according to their morphology and depending on their association with axons. Strikingly, quantitative assessment revealed that the numbers of both foamy SCs (Figure 3d) and foamy macrophages (Figure 3e) were increased in injured *Cmtm6*-cKo compared with genotype control nerves 7 dpc. At 14 dpc, *Cmtm6*-cKo nerves displayed a trend toward increased numbers of foamy SCs and foamy macrophages that did not reach significance (Figure 3d,e). These data imply that SCs and macrophages cope with an increased load of myelin debris and lipid in injured *Cmtm6*-cKo compared to control nerves. At 3, 28, and 56 dpc, the numbers of foamy cells were indistinguishable between the genotypes and expectedly very low. Together, SCs and macrophages may process more debris in *Cmtm6*-cKo nerves early post-injury as reflected by the increased number of lipid-loaded cells; however, this appears as a dynamic, reversible status without a lasting impact on subsequent recovery.

## 2.6 | Lysosomal and (auto)phagocytotic markers are increased in *Cmtm6*-cKo 7 dpc

Repair SCs clear their own myelin debris by myelinophagy and Tyro3/Axl/Mer (TAM)-receptor-mediated phagocytosis (Gomez-Sanchez et al., 2015; Lutz et al., 2017). Considering the increased numbers of foamy SCs and macrophages in *Cmtm6*-cKo mice early post-injury, we extended their assessment using immunohistochemistry on sectioned *Cmtm6*-cKo and control sciatic nerves 7 dpc. Indeed, when detecting lysosomal and phagocytosis markers (LAMP1 and CD68), we observed an overall increase in both LAMP1- (Figure 4a) and CD68-immunolabeling (Figure 4b) in injured *Cmtm6*-cKo compared with genotype control nerves. When detecting the autophagy marker LC3 (microtubule-associated protein 1 light chain 3, MAP1LC3), we found an overall increase in injured *Cmtm6*-cKo compared with genotype control nerves (Figure 4c,d). When co-immunolabeling LC3 with either CD68 (phagocytosis marker, preferentially but not exclusively labelling macrophages; Figure 4c) or SOX10 (labelling SCs; Figure 4d) we found considerable overlap with either marker. This implies that autophagy takes place in both cell types in injured *Cmtm6*-cKo nerves. Notably, non-injured nerves of both *Cmtm6*-cKo and control mice were virtually devoid of immunolabeling for these lysosomal and (auto)phagocytotic markers (Figure 4e). These results thus imply that SCs and macrophages display enhanced (auto)phagocytic properties when SCs lack CMTM6.

Taken together, we established a mild nerve compression model (Figure 1) that results in a shift toward smaller axonal diameters (Figure 1f, Figure S5B–D) without complete degeneration of the entire nerve (Figure 1d). Unexpectedly, in our previously established (Eichel et al., 2020) model of enlarged axonal diameters (*Cmtm6*-cKo mice), the early response to injury 7 dpc involves a shift toward axonal diameters even smaller than in control mice (Figure 2a). This is accompanied by fewer myelinated axons and enhanced axonal pathology (Figure 2b), an increased number of foamy cells (Figure 3), increased immunolabeling for lysosomal and (auto)phagocytotic markers (Figure 4), reduced abundance of transcripts associated with myelination, lipid export and phagocytosis (Figure S5), and reduced grip strength (Figure S3C). While functional recovery is not ameliorated in *Cmtm6*-cKo mice, our data support the concept that larger axons are more vulnerable to mechanical injury.

## 3 | DISCUSSION

We previously identified CMTM6 as an adaxonal SC protein restricting radial axonal growth (Eichel et al., 2020); mice lacking CMTM6 specifically from SCs display enlarged diameters of peripheral axons. In the current study, we developed a comparatively mild sciatic nerve compression injury model. By applying nerve compression to *Cmtm6*-cKo mice, we tested two hypotheses. First, we scrutinized if the increase of axonal diameters caused by CMTM6-deficiency enhances functional recovery after nerve injury by counteracting the injury-dependent reduction of axonal diameters; this hypothesis was not supported by our data. Second, we tested if axons of larger diameters

are more susceptible to mechanical trauma, thereby contributing to the shift toward smaller axonal diameters after nerve injuries that was previously observed (Goodrum et al., 2000; Ikeda & Oka, 2012; Li et al., 2019; Schröder, 1972; Stassart et al., 2013; Tseng et al., 2016). Indeed, our data support the view that larger peripheral axons are more vulnerable toward mechanical trauma.

According to the classification of nerve trauma by Sunderland, more severe nerve crush injury models are categorized as grade III or grade IV, affecting more than 90% of all axons (Wallerian degeneration and demyelination) and potentially disrupting endo- and perineurium (Menorca et al., 2013; Sunderland, 1951). On the other hand, classical compression injuries fall in the category of neuropraxia or grade I axonotmesis injuries with focal demyelination but no axonal or connective tissue damage. More prolonged chronic compression models also cause a form of Wallerian degeneration at later stages (Gupta & Steward, 2003; O'Brien et al., 1987). The nerve compression injury model established here caused pathological signs in a minority of axons in the first week after injury, sparing the complete degeneration of the entire nerve. Our nerve compression also caused limited myelin pathology and mild functional impairment early post-injury; the model thus classifies as axonotmesis grade II nerve trauma (Menorca et al., 2013) in which we observed a predominant loss of axons with mid-to-large diameters (4.5–6  $\mu\text{m}$ ). *Cmtm6*-cKo nerves displayed enhanced pathology, and the injury-dependent decrease in the number of larger diameter axons (>6  $\mu\text{m}$ ) was even enhanced early post-injury. The observed pathological changes largely normalized by 28 dpc when axonal regeneration and remyelination occur (Menorca et al., 2013; Nocera & Jacob, 2020).

Considering that (1) axons display a shift toward smaller diameters in our mild nerve compression model, (2) *Cmtm6*-cKo mice before injury display a shift toward larger axonal diameters and (3) early post-injury present with even smaller axonal diameters and an increased number of pathological profiles that (4) coincide with an enhanced immune response, we believe that the enlargement of the diameters of peripheral axons in *Cmtm6*-cKo mice enhances the vulnerability to mechanical impact. The concept that axons of larger diameters are more susceptible to becoming pathological and to degenerate after injury has been previously suggested based on observations in demyelinating/neurodegenerative disorders in both PNS and CNS (Fujimura et al., 1991; Li, 2015; Lovas et al., 2000; Vavlitou et al., 2010), traumatic brain injuries (Alexandris et al., 2022; Mierzwa et al., 2014), nerve compression injuries (Strain & Olson, 1975), and during aging in the PNS (Chase et al., 1992; Fogarty & Sieck, 2023). Our data are also in agreement with a recent report that a partial nerve crush injury spares small-diameter axons from degenerating and preserves afferent fiber innervation with the skin. The observations likely represent a risk for the development of neuropathic pain, a clinical condition for which effective therapies are not existent (Kim et al., 2023). Thus, mild compression injury or partial crush models may be well suited to model particular human peripheral nerve injury types and have the potential to support the translation from animal to the clinic.

Why are large diameter axons more susceptible to mechanical trauma than small diameter axons? Similar findings regarding axonal

diameters after nerve compression have previously been explained by the Law of Laplace (Strain & Olson, 1975), which—originally phrased in the early 19th century by both Pierre Simon Marquis de Laplace and Thomas Young—states that the tension in the wall of a cylinder is proportional to the difference between internal and external pressures and the radius of the cylinder ( $T = P \times R$ ). A large diameter axon displays an increased wall area, whereby the mechanical stress in force per unit area is increased, initiating a deformation process that will eventually lead to faster/increased degeneration (Strain & Olson, 1975). We note that the application of the Law of Laplace to axon sizes after nerve injury remains to be proven experimentally. Notably, however, several cytoskeletal elements, including neurofilaments, submembrane actin/spectrin-rings, and alpha-adducin, are involved in the development and maintenance of axons, including axonal diameters (Costa et al., 2018; Leite et al., 2016). However, it remains speculative if these molecules are differently expressed in differently sized myelinated axons and thereby may contribute to susceptibility to injury.

Peripheral nerves have a remarkable regenerative capacity after injuries when compared to the CNS. However, this recovery is often slow and incomplete, deteriorating with age in both rodents and humans (Höke, 2006; Scheib & Höke, 2016; Verdú et al., 2000). Common impairments include reduced axonal diameters and hypomyelination (Goodrum et al., 2000; Ikeda & Oka, 2012; Li et al., 2019; Schröder, 1972; Tseng et al., 2016). The interaction between SCs and axons is crucial for sufficient regeneration and remyelination (Stassart & Woodhoo, 2021). For example, the growth factor neuregulin-1 is essential for SC-mediated, axon diameter-dependent myelination during development and post-injury myelin sheath restoration (Fricker et al., 2011; Michailov et al., 2004; Stassart et al., 2013; Taveggia et al., 2005). Mice lacking CMTM6 in SCs show increased axonal diameters, both non-injured (Eichel et al., 2020) and 8 weeks post-injury. *Cmtm6*-cKo mice did not exhibit enhanced nerve recovery or functional improvement post-compression, implying that CMTM6 depletion in SCs is not a viable therapeutic strategy for enhanced recovery after nerve injury. However, our findings do not entirely dismiss possible benefits of therapeutically increasing axonal diameters for functional outcomes post-injury. For instance, low-intensity ultrasound treatment shown to augment axonal diameters, myelination, and nerve conduction post-injury may hold promise, though its clinical applicability remains uncertain (Acheta et al., 2022; Tseng et al., 2016).

During the first week after injury, SCs begin to break down myelin via both, TAM-receptor-mediated phagocytosis and an autophagic process termed myelinophagy (Gomez-Sanchez et al., 2015; Lutz et al., 2017). Concurrently, they attract macrophages to assist in myelin phagocytosis and debris clearance, facilitating subsequent regeneration (Chen et al., 2015; Vargas & Barres, 2007). Our analysis of injured sciatic nerves revealed lysosomal and lipid accumulations 7–14 dpc, the period during which most myelin is cleared, resulting in lipid accumulations in SCs and macrophages and SC lysosomal activation (Jang et al., 2016; Jung et al., 2011; Lutz et al., 2017; Nocera & Jacob, 2020). Notably, we find an increase in the number of foamy

SCs and macrophages and an increase of CD68, LC3, and LAMP1-immunopositive profiles in injured *Cmtm6*-cKo compared with genotype-control nerves 7 dpc. Considering that *Cmtm6*-cKo mice display larger diameter axons with appropriately thicker myelin sheaths pre-injury and a higher proportion of pathological myelinated axons post-injury, it is plausible that these CMTM6-dependent changes cause lipid accumulations and enhanced (auto)phagocytosis and lysosomal activation.

Since we did not detect particularly striking genotype-dependent differences of relevant marker transcripts by qRT-PCR, including the transcription factor c-Jun that induces trans-differentiation into repair SCs (Arthur-Farraj et al., 2012), and no prolonged neuropathological changes, SCs lacking CMTM6 can principally cope with the increased debris. However, CMTM6 might play additional roles in SC injury response or their interaction with macrophages. Consistent with previous RNA-seq studies, we found reduced *Cmtm6*-mRNA abundance in sciatic nerves post-injury, suggesting a role in normal SC injury responses (Lutz et al., 2022; Yi et al., 2015). Considering that CMTM6-expression declines early after injury and its partial redistribution to the abaxonal SC surface, it is possible that its deletion indirectly affects the immune response via yet-unknown signals. Indeed, its name notwithstanding, CMTM6 lacks a recognizable chemokine-like motif (Burr et al., 2017; Eichel et al., 2020; Mezzadra et al., 2017); a direct immunomodulatory function of CMTM6 in vivo is thus not evident. It is plausible that the adaxonal localization of CMTM6 is required for regulating the diameter of the axon. Its partial redistribution to the abaxonal surface brings CMTM6 into a position in which it may affect neighboring nonaxonal structures, including immune cells.

Interestingly, the cholesterol efflux-related transcript *Abca1* and the phagocytosis marker/fatty acid translocase transcript *Cd36* display a genotype-dependent decrease in *Cmtm6*-cKo nerves upon injury. It is yet unknown whether lipid handling is linked to the increase in the number of foamy cells, if it contributes the observed neuropathology, and/or if it is induced by the presence of more debris. It is noteworthy that a prior genome-wide association study has linked a single nucleotide polymorphism next to the *CMTM6* locus with low-density lipoprotein (LDL) (-cholesterol levels and an increased risk for coronary artery disease (Global Lipids Genetics Consortium, 2013). In addition, in vitro silencing of *CMTM6* in monocyte-derived human macrophages via RNA-interference caused reduced LDL uptake by macrophages (Domschke et al., 2018). Notably, in the CNS of both mice and humans, CMTM6 is also expressed by microglial cells (Zhang et al., 2014), which can phagocytose myelin and become foamy phagocytes in pathological states (Berghoff et al., 2021; Kuhlmann et al., 2017; Van Den Bosch et al., 2022). It will thus be interesting to test in future experiments if CMTM6 affects lipid handling by microglia with possible therapeutic relevance for demyelinating CNS disorders.

### 3.1 | Limitations of the study

In this study, we used a mild compression model to avoid degeneration of all axons and thus complete nerve damage. Notably, compared

to transection of entire nerves, nerve compression causes a more variable degree of pathology and molecular changes, making molecular assessments somewhat more scattered. Yet, our findings support the concept that axons of larger diameters are more vulnerable to mechanical injury, at least in the PNS. We note that the present work assessed entire nerves. At the level of single axons, it remains to be tested if larger diameter axons are indeed more prone to degeneration after mechanical trauma. However, when balancing the use of mice against possible scientific outcomes, other models that allow single axon tracking by in vivo imaging and 3D approaches visualizing the axons in its entirety are probably better suited to approach this question. It will thus be an interesting task for future investigation to visualize the fate of individual axons of different diameters after injury, possibly in zebrafish.

Our study indicates that depleting CMTM6-expression in SCs to increase axonal diameters is not a suitable approach toward enhancing recovery after peripheral nerve injuries. Indeed, *Cmtm6*-cKo mice do not display increased axonal diameters at early post-injury stages, and our comparatively mild compression model targets only a subset of axons in the sciatic nerve. Yet, we believe that other strategies toward increasing axonal diameters including low-intensity ultrasound treatment may well ameliorate therapeutic recovery after nerve injury (Canu et al., 2009; Tseng et al., 2016). However, counteracting CMTM6-function could be useful in other peripheral nerve conditions. For example, mice lacking the gene encoding myelin-associated glycoprotein (MAG) display reduced diameters of peripheral axons (Eichel et al., 2020; Yin et al., 1998). Importantly, we showed that the CMTM6-deficiency-dependent increase of axonal diameters overrides their MAG-deficiency-dependent reduction (Eichel et al., 2020). Notwithstanding that the MAG gene so far has not been reported to cause (when mutated) a neuropathy, this implies that counteracting CMTM6 may emerge as a strategy toward normalizing nerve function in neuropathies caused by anti-MAG antibodies (Lunn et al., 2002) or similar conditions. It will thus be an interesting topic of future research to explore this possibility in neuropathy models. We note that the Tamoxifen-inducible *Cmtm6*<sup>flox/flox</sup>; *Plp*<sup>CreEERT2</sup> model (Eichel et al., 2020) allows temporal control to achieve increased axonal diameters, circumventing developmental effects. Yet, the fact that the nerve injury-dependent decrease of axonal diameters overrides the CMTM6-deficiency-dependent increase, which in turn overrides MAG-deficiency-dependent decrease, implies the existence of a hierarchy of signals that has not been well understood. This implies that further SC surface molecules are involved in the regulation of axonal diameters but remain to be discovered.

## 4 | CONCLUSION

Increasing the diameters of peripheral axons by depleting the *Cmtm6* gene from SCs or otherwise counteracting CMTM6 is not suited as concept toward enhancing the regeneration of peripheral nerves after injury. On the contrary, our observations support the concept that larger diameter axons are susceptible to mechanical nerve injury. It

will be relevant to understand the features that make particular axons more vulnerable when aiming to prevent them from degenerating.

## 5 | METHODS

### 5.1 | Mouse models

Mice lacking expression of CMTM6 in SCs (*Cmtm6<sup>flox/flox</sup>;Dhh<sup>Cre</sup>* mice; also termed *Cmtm6*-cKo) were previously reported (Eichel et al., 2020), and genotypes were determined by genomic PCR as described (Eichel et al., 2020). Experimental mutant mice were operated on and analyzed together with littermate controls (*Cmtm6<sup>flox/flox</sup>*) as far as possible. Mice were bred and kept in the mouse facility of the Max Planck Institute for Multidisciplinary Sciences (MPINAT), Göttingen, Germany. All animal experiments were performed in accordance with the German animal protection law (TierSchG) and approved by the Niedersächsisches Landesamt für Verbraucherschutz und Lebensmittelsicherheit (LAVES) under license 33.19-42502-04-19/3077. All procedures were supervised by the animal welfare officer and the animal welfare committee for the MPINAT. The animal facility at the MPINAT is registered according to §11 Abs. 1 TierSchG.

### 5.2 | Peripheral nerve compression injury

Adult mice at the age of 3.5–4 months were anesthetized with a mixture of Fentanyl (Dechra Veterinary Products) (0.05 mg/kg), Midazolam (Ratiopharm, Ulm, Germany) (5 mg/kg), Medetomidine (Alfabet, Neumunster, Germany) (0.5 mg/kg) and diluted in 1 M NaCl (Merck, Darmstadt, Germany) by intraperitoneal injection. After mice were anesthetized, to prevent drought of their eyes, a small amount of Bepanthen ointment (Bayer, Leverkusen, Germany) was applied. A small incision was made distally of the sciatic notch at the left leg, and the sciatic nerve was exposed. The nerve was compressed at the mid-femoral level, 2–3 mm proximally where the sciatic nerve is branching toward the tibial, peroneal, and sural nerve, by a standardized compression with flat, artery forceps (Dumoxel, Dumont WPI, USA) for 15 s. Thereafter, the injury site was sutured (silky, braided, nonabsorbable suture, B. Braun, Melsungen, Germany). Mice were injected subcutaneously with pain medication ([Bayer, Leverkusen, Germany], 0.1 mg/kg diluted in 1 M NaCl) and anesthesia reversal (Atipamezole [Alfabet, Neumunster, Germany] 2.5 mg/kg and Flumazenil [Hexal, Holzkirchen, Germany] 0.5 mg/kg diluted in 1 M NaCl). Post-injury, mice were kept on a warming pad until fully awake; oats, mashed food, and water containing pain medication (1 mL Metamizolnatrium 1 H<sub>2</sub>O 500 mg/mL, 5 g glucose in 100 mL tap water) was provided for a maximum of 1–3 days post-injury. Buprenorphine was injected subcutaneously for a maximum of 30 h post-injury (maximum 2 times per day, every 8 h) in case mice showed any signs of pain. To assess sensory, motor, and functional capabilities, behavioral testing and electrophysiological measurements were performed 7, 14, 28, and 56 dpc. CatWalk™ analysis was performed as described below

with a separate cohort. For morphological and molecular analysis, mice were sacrificed 3, 7, 14, 28, and 56 dpc. The sciatic nerves were dissected, and the part distal to the injury site was processed for histology and molecular analysis.

### 5.3 | Electron microscopy

For conventional transmission electron microscopy (TEM), sciatic nerves of mice were dissected 3, 7, 14, 28, and 56 dpc and postfixed in Karlsson–Schultz fixative (4% PFA, 2.5% glutaraldehyde in 0.1 M phosphate buffer) solution at 4°C until further processing. Thereafter, the sciatic nerves were postfixed with OsO<sub>4</sub> (Science Services, Munich, Germany), dehydrated with ethanol and propyleneoxide by using an automated system (EMTP Leica Microsystems, Wetzlar) and embedded in epoxy resin (Serva). For TEM, ultrathin sections (50 nm) of the distal part of the sciatic nerve were cut with the use of a diamond knife (45°, Diatome Biel, CH) via the PTPC Powertome Ultramicrotome (RMC, Tuscon Arizona, USA) and collected on formvar polyvinyl-coated double-sized slot grids (AGAR Scientific, Essex, UK). UranylLess (Electron Microscopy Science, Hatfield, Panama) was used to contrast ultrathin sections for 15–30 min followed by six subsequent washing steps with ddH<sub>2</sub>O (Patzig et al., 2016; Weil et al., 2019). Samples were examined using EM 912 AB-Omega (Zeiss, Oberkochen, Germany) coupled to a wide-angled dual-speed 2k CCD camera (TRS, Moorenweis, Germany). For quantitative analyses of g-ratio, 20–25 random, nonoverlapping images were taken at 3000× magnification; g-ratio was assessed using ImageJ (Fiji) and calculated as the ratio between axonal Feret diameter and Feret diameter of the corresponding myelin sheath (Fledrich et al., 2014; Patzig et al., 2016). For g-ratios only normal-appearing, non-degenerating/degenerated myelinated axons were analyzed. In total, between 70 and 150 axons per mouse with  $n = 4$  were quantified. All quantifications were performed blinded to the genotype.

### 5.4 | Histology, semithin sections, and axonal diameter determination

Semithin (500 nm) cross-sections of Epon-embedded distal part of the sciatic nerves of indicated genotypes and time points post-injury were obtained using a PTPC Powertome Ultramicrotome, transferred to a glass slide, dried on a warm plate (60°C), and stained by applying methylene blue/azur II (1:1) for 1 min followed by 3× washing with ddH<sub>2</sub>O. Images were acquired at 100× magnification using a bright-field light microscope (Zeiss AxioImager Z1; coupled to Zeiss AxioCam MRc camera; controlled and stitched by Zeiss Zen 1.0 software). Axonal diameters were semiautomatically quantified as previously described (Eichel et al., 2020). Pathological appearing axons were quantified on the same semithin sections using the following characteristics: axonal degeneration, axons filled with myelin debris, Wallerian-type degeneration, axons with myelin tomaculae, and endoaxonal edema. Quantification of macrophages and SCs was performed on the

same semithin sections using the cell counter plugin function of NIH ImageJ (Fiji). Macrophages were quantified according to Forese et al. (2020) and were separated into two categories, that is, (1) foamy, lipid-loaded macrophages and (2) macrophages in proximity to an axon but lacking lipid accumulations. Onion bulb-like, roundish SC profiles were counted as two categories, that is, (1) foamy, lipid-loaded SCs and (2) those lacking lipid accumulations. The number of mice used for the quantification were  $n = 5$  per genotype per time point unless indicated otherwise. All quantifications were performed blinded to the genotype.

## 5.5 | Behavioral analysis

All phenotypical analyses were performed by the same investigator blinded toward genotypes 7, 14, 28, and 56 dpc. To assess motor capabilities, mice were placed once on a metal grid (1 cm grid size) and allowed to run a distance of 2 m while being videotaped. The number of hind limb slips was assessed on a slow-motion video (Eichel et al., 2020). Mice further underwent the grip strength test from 14 dpc onwards. Here, mice were placed on their cage lid, grabbed by their back fur, and allowed to rest their hind limbs on a horizontal bar connected to a gauge, their tail was pulled toward the bar, and the force they use to grab the bar was measured by the gauge in N (newton). A total of 10 replicates were performed (Fledrich et al., 2014). To assess sensory reaction, mice were placed on a hot plate (Leica HI 1220; Nussloch, Germany) which was heated to a constant 52°C and surrounded by a clear acrylic cage (open top). A timer was started once mice were placed on the hot plate, and the time until mice respond with either licking or retracting one of their left hind limbs was stopped and measured as retraction latency. Thereafter, mice were immediately removed from the hot plate and placed back in the home cage. All assessments were performed one mouse at a time, with prior habituation to the room but no training.

Additionally, a variety of gait parameters was assessed using the CatWalk™ XT (CT) system (Noldus, Netherlands). Experimental procedures were as previously described (Heinzel et al., 2020; Kappos et al., 2017; Timotius et al., 2019). Briefly, to minimize stress and induce better performance, mice were first habituated for 1 day and trained for four consecutive days to the CT system. For habituation, each mouse was free to explore and walk freely through the CT system without any rewards. For the training days, mice walked freely through the CT system, and their runs were recorded. An experimental session lasted between 2 and 10 min depending on the speed of the mice (between 10 and 48 cm/s). The CT system recorded three consecutive runs indicated by mice walking the whole distance of the walkway without stopping. From the training days, the day with the fastest run was used for non-injured control. After the induction of sciatic nerve injury on the left hind limb, mice were placed at the CT at 1, 3, 7, 14, 28, and 56 dpc. The same paradigm was used for recording the experimental days. For data analysis, only mice with an average speed above 15 cm/s were used, since speed is known to affect gait parameters (Batka et al., 2014). All footprint positions for

compliant runs were automatically identified by the system and manually reassessed by an experienced observer. Calculation of the SFI was used as implemented in the CT system. Toe spread, intermediate toe spread and print length were measured both for the injured and non-injured side for each consecutive run; only paw prints including four to five digits were included in the analysis. All analyses were performed blinded to the genotype.

## 5.6 | NCV measurement

Standard electroneurography was performed on the left, injured hind limb of *Cmtm6*-cKo and genotype control mice 14, 28, and 56 dpc. Mice were anesthetized with an intraperitoneal injection of ketamine hydrochloride/xylazine hydrochloride (100/8 mg/kg BW). A fine pair of subdermal needle electrodes (Technomed Europe, Maastricht, Netherlands) was placed subcutaneously along the sciatic nerve close to the sciatic notch for proximal stimulation and another one on the tibial nerve above the area of the ankle for distal stimulation. The ground electrode was placed subcutaneously and close by to the other pairs of electrodes. The Neurosoft Evidence EMG and Omega 2014 software (Schreiber & Tholen Medizintechnik GmbH, Stade) was used for measurements and analysis. Increasing voltage pulses were delivered until supramaximal stimulation was achieved. Compound motor action potential (CMAP) from the foot muscles and both the amplitude and latency were recorded. The distance between the two sites of stimulation was manually measured when the leg was fully stretched, and NCV was calculated from the motor action potential latency measurements over the measured distance.

## 5.7 | Quantitative real-time PCR

mRNA abundances were determined by qRT-PCR using the distal part of the injured or non-injured sciatic nerves of control and *Cmtm6*-cKo mice 7 dpc. To minimize the effects of the surrounding tissue affected by the nerve injury, the epineurium was carefully removed for each nerve before freezing samples at  $-80^{\circ}\text{C}$ . Thereafter, frozen tissue was homogenized in TRIzol (Life Technologies, Thermo Fischer Scientific, St. Leon-Rot, Germany), RNA was extracted and purified using RNeasy Miniprep kit (Qiagen, Portland, USA), and Agilent RNA 6000 Nano kit and Agilent 2100 Bioanalyser (Agilent Technologies, Santa Clara, California, USA) were used to evaluate the integrity of the purified RNA. Next, cDNA was synthesized using random nonamer primers and SuperScript III RNA H Reverse Transcriptase (Invitrogen, Karlsruhe, Germany). qRT-PCR was performed using Power SYBR Green PCR Master Mix (Promega, Fitchburg, USA) and Light Cycler 480II (Roche Diagnostics GmbH, Mannheim, Germany). The abundance of mRNAs was analyzed in relation to the mean of the standards, which did not differ between genotypes. Four biological replicates with four technical replicates each were used. Statistical analysis was performed in GraphPad Prism 6.0. Primers were intron-spanning, and sequences are listed in Table 1.

**TABLE 1** Primer sequences.

Gene	Sequence (5'-3'; forward–reverse)
<i>Hprt</i>	TCCTCCTCAGACCGCTTTT– CCTGGTTCATCATCGCTAATC
<i>Rplp0</i>	GATGCCAGGAAGACAG– ACAATGAAGCATTTTGGATAATCA
<i>Rps13</i>	CGAAAGCACCTTGAGAGGAA–TTCCAATTAGGTGGGAGCAC
18S	AAATCAGTTATGGTCTTTGGTC– GCTCTAGAATTACCACAGTTATCCAA
<i>Cmtm6</i>	GATACTGGAAAAGTCAAGTCATCG– AATGGGTGGAGACAAAATGA
<i>Sox2</i>	TCCAAAACTAATCACAAATCG– GAAGTGCAATGGGATGAAAA
<i>cJun</i>	GGGTGACATCATGGCTATTTT– TCCAGCCTGAGCTCAACACTT
<i>Mag</i>	TCTACCCGGATTGTCACCTG–GCAGCCTCCTCAGATCC
<i>Pmp22</i>	GCGGTGCTAGTGTGCTCTT–TCAGTCGTGTGCCATTACCC
<i>Aif1</i>	TGTTTTCTCCTCATACATCAGAATC– CCGAGGAGACGTTTCAGCTAC
<i>Lamp2</i>	TGGAGATCCTAACGTTGACTTG–GGCCAGATCCACGACAGT
<i>Trem2</i>	ACAGCACCTCCAGGAATCAAG–ACAGCCCAGAGGATGC
<i>Mrc1</i>	CCACAGCATTGAGGAGTTTG–ACAGCTCATATTTGGCTCA
<i>Scarb1</i>	GCCCATCATCTGCCAACT–TCCTGGGAGCCCTTTTACT
CD36	TTGTACCTATACTGTGGCTAAATGAGA– CTTGTGTTTTGAACATTTCTGCTT
<i>ApoE</i>	GACCCTGGAGGCTAAGGACT–AGAGCCTTCATCTTCGCAAT
<i>Abca1</i>	CTGTTTCCCAACTTCTG–TCTGCTCCATCTCTGCTTTC
<i>Abcg1</i>	TCTTTGATGAGCCACCAGT–GGGCCAGTCTTTCATCA
<i>Tgfb1</i>	TGGAGCAACATGTGGAACCT–CAGCAGCCGGTTACCAAG
<i>Nos2</i>	TGAACCTGAGCGAGGAGCA– TTCATGATAACGTTTCTGCTCT
<i>Arg1</i>	AAGGAAAGTCCAGATGTACC– GCAAGCCAATGTACACGATG
<i>Ii10</i>	GGTTGCCAAGCCTTATCGGA–ACCTGCTCCACTGCCTTGCT

## 5.8 | Immunohistochemistry

For immunolabeling of cryosections, injured sciatic nerves were dissected from mice 7 dpc and cut at the injury site. For non-injured controls, the right sciatic nerve was collected and halved as well. Both the sciatic nerve parts distal and proximal to the injury (or half part) were immersion fixed in 4% PFA for 1 h and afterwards transferred to sucrose buffer (10% 1 h; 20% and 30% in PBS overnight at 4°C). Using Tissue-Tek O.C.T. (Sakura, Staufen, Germany), the nerve pieces were embedded in plastic chambers and stored at –20°C until further processing. A 10–12- $\mu$ m-thick cross-sections of the distal part were cut using a cryostat (Reichert Jung Cryocut 1800, Wetzlar, Germany), and 3–4 cross-sections were collected on Superfrost Plus microscope glass slides (Thermo Fischer Scientific). Slides were dried for 10–15 min at RT and stored at –20°C until further use.

Immunolabeling was performed using 200–300  $\mu$ L volume per slide with the following steps being applied: slides were incubated in

4% PFA for 5 min, followed by 5 min 100% methanol, washed three times for 5 min in PBS followed by 1 h blocking buffer (PBS, 10% horse serum, and 0.1% Tween-20) at RT. Primary antibodies were applied in the blocking buffer overnight at 4°C. Samples were washed in PBS 3  $\times$  5 min, and secondary antibodies diluted in blocking buffer (1:1000) were applied for approximately 1 h at RT. Thereafter, samples were washed with PBS 3  $\times$  5, incubated with DAPI (Thermo Scientific, Waltham, USA) for 5–10 min, and washed again twice for 5 min in PBS and 2  $\times$  30 s in ddH<sub>2</sub>O before being mounted using Aqua-Poly/Mount (Polysciences, Eppelheim, Germany). Antibodies were specific for MAG (clone 513; Chemicon, Cat# MAB1567; 1:50), CMTM6 (OriGene, Cat# TA322304, 1:200), LAMP1 (BD Biosciences, Cat#553792, 1:200), SOX10 (RD Systems Cat# AF2864, 1:300), LC3 (Novusbio, Cat# NB100-2220, 1:300), and CD68 (Serotec, Cat# MCA1957 1:300). Secondary antibodies were diluted 1:1000 and were either donkey  $\alpha$ -mouse-Alexa488, donkey  $\alpha$ -rabbit-Alexa488, donkey  $\alpha$ -goat-Alexa488, donkey  $\alpha$ -mouse-Alexa555, donkey  $\alpha$ -rabbit-Alexa555, donkey  $\alpha$ -mouse-Dylight633, donkey  $\alpha$ -rat-Dylight633, or donkey  $\alpha$ -rabbit-Alexa633 (Invitrogen).

For overview images, slides were imaged at 10 $\times$  using Axio Observer Z2 (Zeiss) and ZEN Software. For images at a higher magnification, slides were imaged using the confocal microscope LSM880 (Zeiss, Oberkochen, Germany). The signal was collected with the objective Plan-Apochromat 40 $\times$ /1.4 Oil DIC M27 using oil (Immersion Oil 518 F, Zeiss, Oberkochen, Germany) and an additional zoom of 1.7 or 2.5. To observe the samples with the light source Colibri (Zeiss, Oberkochen, Germany), an FS90 filter was used. DAPI was excited at 405, and the signal was collected between 415 and 510 nm. Alexa 555 was excited with a DPSS 561-10 laser at an excitation of 561 nm, and the signal was collected between 562 and 624 nm. Then, Dylight 633 was excited with a HeNe633 laser at an excitation of 633 nm and an emission between 647 and 679 nm. Finally, the MBS 488/561/633 beam splitter was used to detect Alexa 555 and Dylight 633 and MBS-405 for DAPI, respectively. Fiji, Photoshop, and Adobe Illustrator were used to export, process, and assemble the images.

## 5.9 | Statistics and reproducibility

Statistical analyses were mainly performed in GraphPad Prism (GraphPad Software, Inc., San Diego, USA). Data are mainly shown as bar graphs or dot plots with mean  $\pm$  SD (error bars). Data points in graphs represent individual mice, except for data points representing axon/myelin profiles in data clouds showing g-ratios in Figure S2. The exact sample size/number of mice is given in the figures and/or figure legends. Data distribution was assumed to be normal but not formally tested. Outlier tests were performed on all data using the built-in function in GraphPad except for axonal diameters. For comparing two groups, an unpaired two-tailed Student's *t*-test was applied. For CatWalk™ data, since the *n* number slightly differs between time points, a mixed-effects model with Geisser–Greenhouse correction and Sidak's multiple comparisons test was used instead of a repeated measure two-way analysis of variance (ANOVA). For qRT-PCR, one-way

ANOVA with Tukey posttest was performed. RStudio (<https://www.rstudio.com/>, version 3.4.1) was used to statistically assess relative frequency distributions of axonal diameters as previously described (Eichel et al., 2020, <https://github.com/MariaEichel/FrequencyDistributions>). Visualization of axonal diameter frequency distributions was performed by using GraphPad Prism with all measured axonal diameter values per mouse grouped respectively to their genotype. A  $p$ -value of  $<.05$  was considered significant in all tests. Significance levels are represented as n.s. = non-significant,  $*p < .05$ ,  $**p < .01$ , and  $***p < .001$  with exact  $p$ -values given in the figure legends. Representative electron micrographs were chosen from the images obtained from 3 to 5 different biological replicates per genotype. Micrographs are representative of 3–5 biological replicates per genotype. For immunofluorescence labelling and confocal microscopy, representative images were chosen from 2 to 3 independent experiments.

## AUTHOR CONTRIBUTIONS

**V.I.G.:** Investigation; methodology; writing—review and editing. **S.B.:** Investigation; methodology; supervision; writing—review and editing. **D.K.:** Investigation; methodology; writing—review and editing. **S.H.:** Writing—review and editing. **K.L.H.M.P.:** Writing—review and editing. **W.M.:** Methodology; writing—review and editing. **K.A.N.:** Writing—review and editing. **R.F.:** Supervision; methodology; writing—review and editing. **H.B.W.:** Conceptualization; supervision; writing—review and editing; funding. **M.A.E.V.:** Conceptualization; investigation; supervision; writing—original draft; writing—review and editing.

## ACKNOWLEDGMENTS

We thank R. Jung for technical support, T. Buscham, L. Linhoff, S. Siems, L. Spieth and T. Sun for discussions, M. Peine for mouse husbandry, and J.C. Heinzel for support with the CatWalk™ system. V.I.G. and S.H. thank the International Max Planck Research School for Genome Science (IMPRS-GS) for support. K.A.N. holds a European Research Council (ERC) Advanced Grant (“MyeliNano” to K.A.N.). M. A.E.V. is recipient of a Walter-Benjamin Fellowship by the Deutsche Forschungsgemeinschaft (DFG grant 493410640 to M.A.E.V.) and an UKRI postdoctoral fellowship (EP/Y029577/1 to M.A.E.V.). This work was supported by the Deutsche Forschungsgemeinschaft (DFG grant WE 2720/5-1 to H.B.W.). Open Access funding enabled and organized by Projekt DEAL.

## CONFLICT OF INTEREST STATEMENT




The authors declare no competing interests.

## DATA AVAILABILITY STATEMENT

All relevant data are included in the main paper or supplemental files.

## ORCID

Vasiliki-Ilya Gargareta  <https://orcid.org/0000-0002-6673-0714>  
 Stefan A. Berghoff  <https://orcid.org/0000-0002-3794-7295>  
 Doris Krauter  <https://orcid.org/0000-0002-1779-093X>  
 Sophie Hümmert  <https://orcid.org/0009-0001-3787-2043>

Katy L. H. Marshall-Phelps  <https://orcid.org/0000-0001-6275-5941>  
 Wiebke Möbius  <https://orcid.org/0000-0002-2902-7165>  
 Klaus-Armin Nave  <https://orcid.org/0000-0001-8724-9666>  
 Robert Fledrich  <https://orcid.org/0000-0001-5323-7958>  
 Hauke B. Werner  <https://orcid.org/0000-0002-7710-5738>  
 Maria A. Eichel-Vogel  <https://orcid.org/0000-0002-9925-7249>

## REFERENCES

- Acheta, J., Stephens, S. B. Z., Belin, S., & Poitelson, Y. (2022). Therapeutic low-intensity ultrasound for peripheral nerve regeneration—A Schwann cell perspective. *Frontiers in Cellular Neuroscience*, 15, 812588. <https://doi.org/10.3389/fncel.2021.812588>
- Alexandris, A. S., Wang, Y., Frangakis, C. E., Lee, Y., Ryu, J., Alam, Z., & Koliatsos, V. E. (2022). Long-term changes in axon calibers after injury: Observations on the mouse corticospinal tract. *International Journal of Molecular Sciences*, 23(13), 7391. <https://doi.org/10.3390/ijms23137391>
- Arthur-Farraj, P. J., Latouche, M., Wilton, D. K., Quintes, S., Chabrol, E., Banerjee, A., Woodhoo, A., Jenkins, B., Rahman, M., Turmaine, M., Wicher, G. K., Mitter, R., Greensmith, L., Behrens, A., Raivich, G., Mirsky, R., & Jessen, K. R. (2012). c-Jun reprograms Schwann cells of injured nerves to generate a repair cell essential for regeneration. *Neuron*, 75(4), 633–647. <https://doi.org/10.1016/j.neuron.2012.06.021>
- Batka, R. J., Brown, T. J., Mcmillan, K. P., Meadows, R. M., Jones, K. J., & Haulcomb, M. M. (2014). The need for speed in rodent locomotion analyses: The need for speed. *The Anatomical Record*, 297(10), 1839–1864. <https://doi.org/10.1002/ar.22955>
- Berghoff, S. A., Spieth, L., Sun, T., Hosang, L., Schlaphoff, L., Depp, C., Düking, T., Winchenbach, J., Neuber, J., Ewers, D., Scholz, P., van der Meer, F., Cantuti-Castelvetri, L., Sasmita, A. O., Meschkat, M., Ruhwedel, T., Möbius, W., Sankowski, R., Prinz, M., ... Saher, G. (2021). Microglia facilitate repair of demyelinated lesions via post-squalene sterol synthesis. *Nature Neuroscience*, 24(1), 47–60. <https://doi.org/10.1038/s41593-020-00757-6>
- Bilbao, J. M., & Schmidt, R. E. (2015). *Biopsy diagnosis of peripheral neuropathy*. Springer International Publishing. <https://doi.org/10.1007/978-3-319-07311-8>
- Burr, M. L., Sparbier, C. E., Chan, Y. C., Williamson, J. C., Woods, K., Beavis, P. A., Lam, E. Y. N., Henderson, M. A., Bell, C. C., Stolzenburg, S., Gilan, O., Bloor, S., Noori, T., Morgens, D. W., Bassik, M. C., Neeson, P. J., Behren, A., Darcy, P. K., Dawson, S.-J., ... Dawson, M. A. (2017). CMTM6 maintains the expression of PD-L1 and regulates anti-tumour immunity. *Nature*, 549(7670), 101–105. <https://doi.org/10.1038/nature23643>
- Canu, M.-H., Carnaud, M., Picquet, F., & Goutebroze, L. (2009). Activity-dependent regulation of myelin maintenance in the adult rat. *Brain Research*, 1252, 45–51. <https://doi.org/10.1016/j.brainres.2008.10.079>
- Chase, M. H., Kerch Engelhardt, J., Adinolfi, A. M., & Chirwa, S. S. (1992). Age-dependent changes in cat masseter nerve: An electrophysiological and morphological study. *Brain Research*, 586, 279–288. [https://doi.org/10.1016/0006-8993\(92\)91637-T](https://doi.org/10.1016/0006-8993(92)91637-T)
- Chen, P., Piao, X., & Bonaldo, P. (2015). Role of macrophages in Wallerian degeneration and axonal regeneration after peripheral nerve injury. *Acta Neuropathologica*, 130(5), 605–618. <https://doi.org/10.1007/s00401-015-1482-4>
- Chen, Z.-L., Wei-Ming, Y., & Strickland, S. (2007). Peripheral regeneration. *Annual Review of Neuroscience*, 30(1), 209–233. <https://doi.org/10.1146/annurev.neuro.30.051606.094337>
- Chinetti, G., Lestavel, S., Bocher, V., Remaley, A. T., Neve, B., Torra, I. P., Teissier, E., Minnich, A., Jaye, M., Duverger, N., Brewer, H. B., Fruchart, J. C., Clavey, V., & Staels, B. (2001). PPAR-alpha and PPAR-gamma activators induce cholesterol removal from human macrophage



- foam cells through stimulation of the ABCA1 pathway. *Nature Medicine*, 7(1), 53–58. <https://doi.org/10.1038/83348>
- Costa, A. R., Pinto-Costa, R., Sousa, S. C., & Sousa, M. M. (2018). The regulation of axon diameter: From axonal circumferential contractility to activity-dependent axon swelling. *Frontiers in Molecular Neuroscience*, 11, 319. <https://doi.org/10.3389/fnmol.2018.00319>
- Domschke, G., Linden, F., Pawig, L., Hafner, A., Akhavanpoor, M., Reymann, J., Doesch, A. O., Erbel, C., Weber, C., Katus, H. A., Noels, H., Erfle, H., Gleissner, C. A., & Runz, H. (2018). Systematic RNA-interference in primary human monocyte-derived macrophages: A high-throughput platform to study foam cell formation. *Scientific Reports*, 8(1), 10516. <https://doi.org/10.1038/s41598-018-28790-3>
- Eichel, M. A., Gargareta, V. I., D'Este, E., Fledrich, R., Kungl, T., Buscham, T. J., Luders, K. A., Miracle, C., Jung, R. B., Distler, U., Kusch, K., Möbius, W., Hülsmann, S., Tenzer, S., Nave, K.-A., & Werner, H. B. (2020). CMT6 expressed on the adaxonal Schwann cell surface restricts axonal diameters in peripheral nerves. *Nature Communications*, 11(1), 4514. <https://doi.org/10.1038/s41467-020-18172-7>
- Fledrich, R., Stassart, R. M., Klink, A., Rasch, L. M., Prukop, T., Haag, L., Czesnik, D., Kungl, T., Abdelaal, T. A. M., Keric, N., Stadelmann, C., Brück, W., Nave, K.-A., & Sereda, M. W. (2014). Soluble neuregulin-1 modulates disease pathogenesis in rodent models of Charcot-Marie-Tooth disease 1A. *Nature Medicine*, 20(9), 1055–1061. <https://doi.org/10.1038/nm.3664>
- Fogarty, M. J., & Sieck, G. C. (2023). Aging affects the number and morphological heterogeneity of rat phrenic motor neurons and phrenic motor axons. *Physiological Reports*, 11(2), e15587. <https://doi.org/10.14814/phy2.15587>
- Fontana, X., Hristova, M., Da Costa, C., Patodia, S., Thei, L., Makwana, M., Spencer-Dene, B., Latouche, M., Mirsky, R., Jessen, K. R., Klein, R., Raivich, G., & Behrens, A. (2012). c-Jun in Schwann cells promotes axonal regeneration and motoneuron survival via paracrine signaling. *Journal of Cell Biology*, 198, 127–141. <https://doi.org/10.1083/jcb.201205025>
- Forese, M. G., Pellegatta, M., Canevazzi, P., Gullotta, G. S., Podini, P., Rivellini, C., Previtali, S. C., Bacigaluppi, M., Quattrini, A., & Taveggia, C. (2020). Prostaglandin D2 synthase modulates macrophage activity and accumulation in injured peripheral nerves. *Glia*, 68(1), 95–110. <https://doi.org/10.1002/glia.23705>
- Van Den Bosch, A., Fransen, N., Mason, M., Rozemuller, A. J., Teunissen, C., Smolders, J., & Huitinga, I. (2022). Neurofilament light chain levels in multiple sclerosis correlate with lesions containing foamy macrophages and with acute axonal damage. *Neurology Neuroimmunology & Neuroinflammation*, 9(3), e1154. <https://doi.org/10.1212/NXI.0000000000001154>
- Fricker, F. R., Lago, N., Balarajah, S., Tsantoulas, C., Tanna, S., Zhu, N., Fageiry, S. K., Jenkins, M., Garratt, A. N., Birchmeier, C., & Bennett, D. L. H. (2011). Axonally derived neuregulin-1 is required for remyelination and regeneration after nerve injury in adulthood. *Journal of Neuroscience*, 31(9), 3225–3233. <https://doi.org/10.1523/JNEUROSCI.2568-10.2011>
- Fujimura, H., Lacroix, C., & Said, G. (1991). Vulnerability of nerve fibers to ischaemia: A quantitative light and electron microscope study. *Brain*, 114(4), 1929–1942. <https://doi.org/10.1093/brain/114.4.1929>
- Global Lipids Genetics Consortium. (2013). Discovery and refinement of loci associated with lipid levels. *Nature Genetics*, 45(11), 1274–1283. <https://doi.org/10.1038/ng.2797>
- Gomez-Sanchez, J. A., Carty, L., Iruarrizaga-Lejarreta, M., Palomo-Irigoyen, M., Varela-Rey, M., Griffith, M., Hantke, J., Macias-Camara, N., Azkargorta, M., Aurrekoetxea, I., de Juan, V. G., Jefferies, H. B. J., Aspichueta, P., Elortza, F., Aransay, A. M., Martínez-Chantar, M. L., Baas, F., Mato, J. M., Mirsky, R., ... Jessen, K. R. (2015). Schwann cell autophagy, myelinophagy, initiates myelin clearance from injured nerves. *Journal of Cell Biology*, 210(1), 153–168. <https://doi.org/10.1083/jcb.201503019>
- Goodrum, J. F., Brown, J. C., Fowler, K. A., & Bouldin, T. W. (2000). Axonal regeneration, but not myelination, is partially dependent on local cholesterol reutilization in regenerating nerve. *Journal of Neuropathology & Experimental Neurology*, 59(11), 1002–1010. <https://doi.org/10.1093/jnen/59.11.1002>
- Grajchen, E., Wouters, E., Van De Haterd, B., Haidar, M., Hardonnière, K., Dierckx, T., Van Broeckhoven, J., Erens, C., Hendrix, S., Kerdine-Römer, S., Hendriks, J. J. A., & Bogie, J. F. J. (2020). CD36-mediated uptake of myelin debris by macrophages and microglia reduces neuroinflammation. *Journal of Neuroinflammation*, 17(1), 224. <https://doi.org/10.1186/s12974-020-01899-x>
- Gupta, R., & Steward, O. (2003). Chronic nerve compression induces concurrent apoptosis and proliferation of Schwann cells. *The Journal of Comparative Neurology*, 461(2), 174–186. <https://doi.org/10.1002/cne.10692>
- Heinzel, J. C., Hercher, D., & Redl, H. (2020). The course of recovery of locomotor function over a 10-week observation period in a rat model of femoral nerve resection and autograft repair. *Brain and Behavior*, 10(4), e01580. <https://doi.org/10.1002/brb3.1580>
- Höke, A. (2006). Mechanisms of disease: What factors limit the success of peripheral nerve regeneration in humans? *Nature Clinical Practice Neurology*, 2(8), 448–454. <https://doi.org/10.1038/ncpneuro0262>
- Ikeda, M., & Oka, Y. (2012). The relationship between nerve conduction velocity and fiber morphology during peripheral nerve regeneration. *Brain and Behavior*, 2(4), 382–390. <https://doi.org/10.1002/brb3.61>
- Jang, S. Y., Shin, Y. K., Park, S. Y., Park, J. Y., Lee, H. J., Yoo, Y. H., Kim, J. K., & Park, H. T. (2016). Autophagic myelin destruction by Schwann cells during Wallerian degeneration and segmental demyelination: Autophagy in demyelination. *Glia*, 64(5), 730–742. <https://doi.org/10.1002/glia.22957>
- Jessen, K. R., & Mirsky, R. (2016). The repair Schwann cell and its function in regenerating nerves: Repair Schwann cell and its function in regenerating nerves. *The Journal of Physiology*, 594(13), 3521–3531. <https://doi.org/10.1113/JP270874>
- Jessen, K. R., & Arthur-Farraj, P. (2019). Repair Schwann cell update: Adaptive reprogramming, EMT, and stemness in regenerating nerves. *Glia*, 67(3), 421–437. <https://doi.org/10.1002/glia.23532>
- Jessen, K. R., & Mirsky, R. (2019). The success and failure of the Schwann cell response to nerve injury. *Frontiers in Cellular Neuroscience*, 13, 33. <https://doi.org/10.3389/fncel.2019.00033>
- Jung, J., Cai, W., Jang, S. Y., Shin, Y. K., Suh, D. J., Kim, J. K., & Park, H. T. (2011). Transient lysosomal activation is essential for P75 nerve growth factor receptor expression in myelinated Schwann cells during Wallerian degeneration. *Anatomy & Cell Biology*, 44(1), 41–49. <https://doi.org/10.5115/acb.2011.44.1.41>
- Kappos, E. A., Sieber, P. K., Engels, P. E., Mariolo, A. V., D'Arpa, S., Schaefer, D. J., & Kalbermatten, D. F. (2017). Validity and reliability of the CatWalk system as a static and dynamic gait analysis tool for the assessment of functional nerve recovery in small animal models. *Brain and Behavior*, 7(7), e00723. <https://doi.org/10.1002/brb3.723>
- Kim, H. W., Shim, S. W., Zhao, A. M., Roh, D., Han, H. M., Middleton, S. J., Kim, W., Chung, S., Johnson, E., Prentice, J., Tacon, M., Koel-Simmelink, M. J. A., Wieske, L., Teunissen, C. E., Bae, Y. C., Bennett, D. L. H., Rinaldi, S., Davies, A. J., & Oh, S. B. (2023). Long-term tactile hypersensitivity after nerve crush injury in mice is characterized by the persistence of intact sensory axons. *Pain*, 164(10), 2327–2342. <https://doi.org/10.1097/j.pain.0000000000002937>
- Kuhlmann, T., Ludwin, S., Prat, A., Antel, J., Brück, W., & Lassmann, H. (2017). An updated histological classification system for multiple sclerosis lesions. *Acta Neuropathologica*, 133(1), 13–24. <https://doi.org/10.1007/s00401-016-1653-y>
- Leite, S. C., Sampaio, P., Sousa, V. F., Nogueira-Rodrigues, J., Pinto-Costa, R., Peters, L. L., Brites, P., & Sousa, M. M. (2016). The Actin-binding protein  $\alpha$ -adducin is required for maintaining axon diameter. *Cell Reports*, 15(3), 490–498. <https://doi.org/10.1016/j.celrep.2016.03.047>



- Li, J. (2015). Molecular regulators of nerve conduction—Lessons from inherited neuropathies and rodent genetic models. *Experimental Neurology*, 267, 209–218. <https://doi.org/10.1016/j.expneurol.2015.03.009>
- Li, L., Li, Y., Fan, Z., Wang, X., Li, Z., Wen, J., Deng, J., Tan, D., Pan, M., Hu, X., Zhang, H., Lai, M., & Guo, J. (2019). Ascorbic acid facilitates neural regeneration after sciatic nerve crush injury. *Frontiers in Cellular Neuroscience*, 13, 108. <https://doi.org/10.3389/fncel.2019.00108>
- Lovas, G., Szilagyi, N., Majtenyi, K., Palkovits, M., & Komoly, S. (2000). Axonal changes in chronic demyelinated cervical spinal cord plaques. *Brain*, 123, 308–317. <https://doi.org/10.1093/brain/123.2.308>
- Lunn, M. P. T., Crawford, T. O., Hughes, R. A. C., Griffin, J. W., & Sheikh, K. A. (2002). Anti-myelin-associated glycoprotein antibodies alter neurofilament spacing. *Brain*, 125(4), 904–911. <https://doi.org/10.1093/brain/awf072>
- Lutz, A. B., & Barres, B. A. (2014). Contrasting the glial response to axon injury in the central and peripheral nervous systems. *Developmental Cell*, 28(1), 7–17. <https://doi.org/10.1016/j.devcel.2013.12.002>
- Lutz, B., Amanda, T. A., Lucas, G. A., Carson, C. C., Zhou, L., Barres, B. A., Buckwalter, M. S., & Sloan, S. A. (2022). An RNA-sequencing transcriptome of the rodent Schwann cell response to peripheral nerve injury. *Journal of Neuroinflammation*, 19(1), 105. <https://doi.org/10.1186/s12974-022-02462-6>
- Lutz, B., Amanda, W.-S. C., Sloan, S. A., Carson, G. A., Lu, Z., Lovelett, E., Sean, P., Bradley Zuchero, J., & Barres, B. A. (2017). Schwann cells use TAM receptor-mediated phagocytosis in addition to autophagy to clear myelin in a mouse model of nerve injury. *Proceedings of the National Academy of Sciences*, 114(38), E8072–E8080. <https://doi.org/10.1073/pnas.1710566114>
- Madduri, S., & Gander, B. (2010). Schwann cell delivery of neurotrophic factors for peripheral nerve regeneration. *Journal of the Peripheral Nervous System*, 15(2), 93–103. <https://doi.org/10.1111/j.1529-8027.2010.00257.x>
- Menorca, R. M. G., Fussell, T. S., & Elfar, J. C. (2013). Nerve physiology. *Hand Clinics*, 29(3), 317–330. <https://doi.org/10.1016/j.hcl.2013.04.002>
- Mezzadra, R., Sun, C., Jae, L. T., Gomez-Eerland, R., De Vries, E., Wei, W., Logtenberg, M. E. W., Slagter, M., Rozeman, E. A., Hofland, I., Broeks, A., Horlings, H. M., Wessels, L. F. A., Blank, C. U., Xiao, Y., Heck, A. J. R., Borst, J., Brummelkamp, T. R., & Schumacher, T. N. M. (2017). Identification of CMTM6 and CMTM4 as PD-L1 protein regulators. *Nature*, 549(7670), 106–110. <https://doi.org/10.1038/nature23669>
- Michailov, G. V., Sereda, M. W., Brinkmann, B. G., Fischer, T. H., Haug, B., Birchmeier, C., Role, L., Lai, C., Schwab, M. H., & Nave, K. A. (2004). Axonal neuregulin-1 regulates myelin sheath thickness. *Science*, 304, 700–703. <https://doi.org/10.1126/science.1095862>
- Mierzwa, A. J., Sullivan, G. M., Beer, L. A., Ahn, S., & Armstrong, R. C. (2014). Comparison of cortical and white matter traumatic brain injury models reveals differential effects in the subventricular zone and divergent sonic hedgehog signaling pathways in neuroblasts and oligodendrocyte progenitors. *ASN Neuro*, 6(5), 175909141455178. <https://doi.org/10.1177/1759091414551782>
- Nocera, G., & Jacob, C. (2020). Mechanisms of Schwann cell plasticity involved in peripheral nerve repair after injury. *Cellular and Molecular Life Sciences*, 77(20), 3977–3989. <https://doi.org/10.1007/s00018-020-03516-9>
- O'Brien, J. P., Mackinnon, S. E., MacLean, A. R., Hudson, A. R., Dellon, A. L., & Hunter, D. A. (1987). A model of chronic nerve compression in the rat. *Annals of Plastic Surgery*, 19(5), 430–435. <https://doi.org/10.1097/0000637-198711000-00008>
- Painter, M. W., Lutz, A. B., Cheng, Y. C., Latremoliere, A., Duong, K., Miller, C. M., Posada, S., Cobos, E. J., Zhang, A. X., Wagers, A. J., Havton, L. A., Barres, B., Omura, T., & Woolf, C. J. (2014). Diminished Schwann cell repair responses underlie age-associated impaired axonal regeneration. *Neuron*, 83(2), 331–343. <https://doi.org/10.1016/j.neuron.2014.06.016>
- Patzig, J., Kusch, K., Fledrich, R., Eichel, M. A., Lüders, K. A., Möbius, W., Sereda, M. W., Nave, K. A., Martini, R., & Werner, H. B. (2016). Proteolipid protein modulates preservation of peripheral axons and premature death when myelin protein zero is lacking. *Glia*, 64(1), 155–174. <https://doi.org/10.1002/glia.22922>
- Quintes, S., Brinkmann, B. G., Ebert, M., Fröb, F., Kungl, T., Arlt, F. A., Tarabykin, V., Huylebroeck, D., Meijer, D., Suter, U., Wegner, M., Sereda, M. W., & Nave, K. A. (2016). Zeb2 is essential for Schwann cell differentiation, myelination and nerve repair. *Nature Neuroscience*, 19(8), 1050–1059. <https://doi.org/10.1038/nn.4321>
- Scheib, J., & Höke, A. (2016). Impaired regeneration in aged nerves: Clearing out the old to make way for the new. *Experimental Neurology*, 284, 79–83. <https://doi.org/10.1016/j.expneurol.2016.07.010>
- Schröder, J. M. (1972). Altered ratio between axon diameter and myelin sheath thickness in regenerated nerve fibers. *Brain Research*, 45(1), 49–65. [https://doi.org/10.1016/0006-8993\(72\)90215-6](https://doi.org/10.1016/0006-8993(72)90215-6)
- Stassart, R. M., Fledrich, R., Velanac, V., Brinkmann, B. G., Schwab, M. H., Meijer, D., Sereda, M. W., & Nave, K. A. (2013). A role for Schwann cell-derived neuregulin-1 in remyelination. *Nature Neuroscience*, 16(1), 48–54. <https://doi.org/10.1038/nn.3281>
- Stassart, R. M., & Woodhoo, A. (2021). Axo-glial interaction in the injured PNS. *Developmental Neurobiology*, 81(5), 490–506. <https://doi.org/10.1002/dneu.22771>
- Strain, R. E., & Olson, W. H. (1975). Selective damage of large diameter peripheral nerve fibers by compression: An application of Laplace's law. *Experimental Neurology*, 47(1), 68–80. [https://doi.org/10.1016/0014-4886\(75\)90237-X](https://doi.org/10.1016/0014-4886(75)90237-X)
- Stratton, J. A., & Shah, P. T. (2016). Macrophage polarization in nerve injury: Do Schwann cells play a role? *Neural Regeneration Research*, 11(1), 53–57. <https://doi.org/10.4103/1673-5374.175042>
- Sunderland, S. (1951). A classification of peripheral nerve injuries producing loss of function. *Brain*, 74(4), 491–516. <https://doi.org/10.1093/brain/74.4.491>
- Tavecchia, C., Zanazzi, G., Petrylak, A., Yano, H., Rosenbluth, J., Einheber, S., Xiaorong, X., Esper, R. M., Loeb, J. A., Shrager, P., Chao, M. V., Falls, D. L., Role, L., & Salzer, J. L. (2005). Neuregulin-1 type III determines the ensheathment fate of axons. *Neuron*, 47, 681–694. <https://doi.org/10.1016/j.neuron.2005.08.017>
- Timotius, I. K., Canneva, F., Minakaki, G., Mocerì, S., Plank, A.-C., Casadei, N., Riess, O., Winkler, J., Klucken, J., Eskofier, B., & von Hörsten, S. (2019). Systematic data analysis and data mining in CatWalk gait analysis by heat mapping exemplified in rodent models for neurodegenerative diseases. *Journal of Neuroscience Methods*, 326, 108367. <https://doi.org/10.1016/j.jneumeth.2019.108367>
- Tseng, K.-C., Li, H., Clark, A., Sundem, L., Zuscik, M., Noble, M., & Elfar, J. (2016). 4-aminopyridine promotes functional recovery and remyelination in acute peripheral nerve injury. *EMBO Molecular Medicine*, 8(12), 1409–1420. <https://doi.org/10.15252/emmm.201506035>
- Vargas, M. E., & Barres, B. A. (2007). Why is Wallerian degeneration in the CNS so slow? *Annual Review of Neuroscience*, 30(1), 153–179. <https://doi.org/10.1146/annurev.neuro.30.051606.094354>
- Vaughan, D. W. (1992). Effects of advancing age on peripheral nerve regeneration. *The Journal of Comparative Neurology*, 323(2), 219–237. <https://doi.org/10.1002/cne.903230207>
- Vavlitou, N., Sargiannidou, I., Markoullis, K., Kyriacou, K., Scherer, S. S., & Kleopa, K. A. (2010). Axonal pathology precedes demyelination in a mouse model of X-linked demyelinating/type I Charcot-Marie tooth neuropathy. *Journal of Neuropathology and Experimental Neurology*, 69(9), 945–958. <https://doi.org/10.1097/NEN.0b013e3181efa658>
- Verdú, E., Ceballos, D., Vilches, J. J., & Navarro, X. (2000). Influence of aging on peripheral nerve function and regeneration. *Journal of the Peripheral Nervous System*, 5(4), 191–208. <https://doi.org/10.1046/j.1529-8027.2000.00026.x>

- Wagstaff, L. J., Gomez-Sanchez, J. A., Fazal, S. V., Otto, G. W., Kilpatrick, A. M., Michael, K., Wong, L. Y., Ma, K. H., Turmaine, M., Svaren, J., Gordon, T., Arthur-Farraj, P., Velasco-Aviles, S., Cabedo, H., Benito, C., Mirsky, R., & Jessen, K. R. (2021). Failures of nerve regeneration caused by aging or chronic denervation are rescued by restoring Schwann cell c-Jun. *eLife*, 10, e62232. <https://doi.org/10.7554/eLife.62232>
- Weil, M.-T., Ruhwedel, T., Meschkat, M., Sadowski, B., & Möbius, W. (2019). Transmission electron microscopy of oligodendrocytes and myelin. In D. A. Lyons & L. Kegel (Eds.), *Oligodendrocytes. Methods in molecular biology* (Vol. 1936, pp. 343–375). Springer New York. [https://doi.org/10.1007/978-1-4939-9072-6\\_20](https://doi.org/10.1007/978-1-4939-9072-6_20)
- Xiao, Y., Faucherre, A., Pola-Morell, L., Heddeston, J. M., Liu, T.-L., Chew, T.-L., Sato, F., Sehara-Fujisawa, A., Kawakami, K., & López-Schier, H. (2015). High-resolution live imaging reveals axon-glia interactions during peripheral nerve injury and repair in zebrafish. *Disease Models & Mechanisms*, 8(6), 553–564. <https://doi.org/10.1242/dmm.018184>
- Ydens, E., Amann, L., Asselbergh, B., Scott, C. L., Martens, L., Sichien, D., Mossad, O., Blank, T., de Prijck, S., Low, D., Masuda, T., Saeys, Y., Timmerman, V., Stumm, R., Ginhoux, F., Prinz, M., Janssens, S., & Guilliams, M. (2020). Profiling peripheral nerve macrophages reveals two macrophage subsets with distinct localization, transcriptome and response to injury. *Nature Neuroscience*, 23(5), 676–689. <https://doi.org/10.1038/s41593-020-0618-6>
- Yi, S., Zhang, H., Gong, L., Jiancheng, W., Zha, G., Zhou, S., Xiaosong, G., & Bin, Y. (2015). Deep sequencing and bioinformatic analysis of lesioned sciatic nerves after crush injury. *PLoS One*, 10(12), e0143491. <https://doi.org/10.1371/journal.pone.0143491>
- Yin, X., Crawford, T. O., Griffin, J. W., Pang Hsien, T., Lee, V. M. Y., Li, C., Roder, J., & Trapp, B. D. (1998). Myelin-associated glycoprotein is a myelin signal that modulates the caliber of myelinated axons. *Journal of Neuroscience*, 18(6), 1953–1962. <https://doi.org/10.1523/jneurosci.18-06-01953.1998>
- Zhang, Y., Chen, K., Sloan, S. A., Bennett, M. L., Scholze, A. R., O'Keefe, S., Phatnani, H. P., Guarnieri, P., Caneda, C., Ruderisch, N., Deng, S., Liddelov, S. A., Zhang, C., Daneman, R., Maniatis, T., Barres, B. A., & Wu, J. Q. (2014). An RNA-sequencing transcriptome and splicing database of glia, neurons, and vascular cells of the cerebral cortex. *Journal of Neuroscience*, 34, 11929–11947. <https://doi.org/10.1523/JNEUROSCI.1860-14.2014>
- Zhou, Y., Miles, J. R., Tavori, H., Lin, M., Khoshbouei, H., Borchelt, D. R., Bazick, H., Landreth, G. E., Lee, S., Fazio, S., & Nottterpek, L. (2019). PMP22 regulates cholesterol trafficking and ABCA1-mediated cholesterol efflux. *The Journal of Neuroscience*, 39(27), 5404–5418. <https://doi.org/10.1523/JNEUROSCI.2942-18.2019>

## SUPPORTING INFORMATION

Additional supporting information can be found online in the Supporting Information section at the end of this article.

**How to cite this article:** Gargareta, V.-I., Berghoff, S. A., Krauter, D., Hümmert, S., Marshall-Phelps, K. L. H., Möbius, W., Nave, K.-A., Fledrich, R., Werner, H. B., & Eichel-Vogel, M. A. (2024). Myelinated peripheral axons are more vulnerable to mechanical trauma in a model of enlarged axonal diameters. *Glia*, 1–18. <https://doi.org/10.1002/glia.24568>